약학박사 학위논문

Hydroxyapatite-binding albumin nanoclusters for enhancing the targeting ability to the bone tumor microenvironment and antitumor effects

골 암의 미세환경에 대한 표적성과 항암 활성 증가를 위해 하이드록시아파타이트에 대한 친화력을 높인 알부민 나노클러스터에 대한 연구

2022년 2월

서울대학교 대학원

약학과 약제과학 전공

강 내 원

Hydroxyapatite-binding albumin nanoclusters for enhancing the targeting ability to the bone tumor microenvironment and antitumor effects

지도교수 김대덕

이 논문을 약학박사 학위논문으로 제출함
2021년 12월

서울대학교 대학원
약학과 약제과학 전공
강 내 원

강내원의 박사 학위논문을 인준함
2022년 1월

위 원 장 정석재 (인)

부 위 원 장 이우인 (인)

위 원 이재영 (인)

위 원 김기택 (인)

위 원 김대덕 (인)

ABSTRACT

Hydroxyapatite-binding albumin nanoclusters for enhancing the targeting ability to the bone tumor microenvironment and antitumor effects

Nae-Won Kang

Department of Pharmaceutical Sciences

The Graduate School

Seoul National University

Malignant bone tumors feature a highly mineralized extracellular matrix, causing microenvironment-induced resistance to drug accumulation. Herein, alendronate-decorated human serum albumin (HSA-AD) nanoclusters (NCs) were developed for targeting hydroxyapatites in the bone tumor microenvironment and enhancing the tumor suppressive effects. Doxorubicin (DOX) was loaded onto the surface of HSA-AD *via* the ball-milling technology, a novel drug-loading method in which the secondary structures of HSA can be preserved at more than 90%, based on circular dichroism analysis. The targeting ability of NCs was confirmed in a novel *in vitro* bone cancer model, wherein hydroxyapatite and collagen, the major components of the bone matrix representing the highly mineralized bone

tumor microenvironment, were co-cultured with HOS/MNNG cells, a human osteosarcoma cell line. The binding affinity of HSA-AD/DOX to hydroxyapatite was evaluated based on DOX binding efficiency; HSA-AD/DOX showed a 5.04-fold higher affinity than HSA/DOX. The enhanced distribution of HSA-AD/DOX to bone tumors was verified in a newly developed mouse model bearing HOS/MNNG tumors with hydroxyapatite beads. HSA-AD/DOX led to a 52.0% increase in tumor accumulation compared to the unmodified NCs (HSA/DOX). This was mainly due to the hydroxyapatite-binding affinity of the AD moiety, which is supported by histological analysis performed on the dissected tumors. Taken together, the targeting ability of HSA-AD/DOX is effectively translated into improved therapeutic efficacy in bone tumor-xenografted mice, suggesting that the developed NCs are a promising delivery system for bone tumor treatment.

Keywords: bone tumors, alendronate, human serum albumin, nanoclusters, hydroxyapatite

Student Number: 2016-22653

Contents

List of Tables

List of Figures

1. Introduction

1.1. Bone tumor

Bone is a type of specialized connective tissue, consisting of different types of bone cells, including osteoblast, osteocyte, and osteoclast [1]. While osteoblasts and osteocytes are engaged in the formation and mineralization of bone, osteoclasts are involved in the resorption of bone tissue. The combination of these cells maintains the homeostasis of bone, called the bone remodeling cycle that replaces old and damaged bone [2]. The cycle is a highly regulated, lifelong process essential for preserving bone integrity and maintaining mineral homeostasis. This process accompanies the production of abundant cytokines and nutrients, which renders bone vulnerable to metastasis.

Bone matrix is composed of inorganic and organic components [2]. While the inorganic component is primarily made of crystalline hydroxyapatites and amorphous calcium phosphate, the organic component contains roughly 20 proteins with type I collagen. Hydroxyapatites are a natural mineral form of calcium apatite with the formula of ($Ca_{10}(PO_4)_6(OH)_2$), and have a specific crystallographic structure, called hexagonal system. The biological hydroxyapatites constitute bone structure up to 50 % by volume and 70 % by mass [1]. Their unique composition and shape allow the bone to be relatively hard and strong with remaining lightweight [2].

Bone tumor is defined as a neoplastic growth of tissue in bone. It destroys normal bone tissue and accompanies severe pain. Bone tumors are classified as “primary bone tumors” which originates in bone or from bone-derived cells and tissues, and “secondary bone tumor” which originates from other sites and sequentially spread to the bone [3]. Secondary bone tumors are metastatic lesions that have spread from other organs, most commonly carcinomas of the breast, lung, and prostate [4]. Common benign tumors include osteoma, osteoid osteoma, osteochondroma, osteoblastoma, enchondroma, giant cell tumor of bone, and aneurysmal bone cyst. Meanwhile, malignant bone tumors include osteosarcoma, chondrosarcoma, Ewing’s sarcoma, and fibrosarcoma [5].

The malignant bone tumor has a specialized tumor microenvironment, characterized as a highly mineralized extracellular matrix [6], similar to that of normal bone. To cure the tumors, different combinations of several anticancer agents, such as doxorubicin (DOX), cisplatin, etoposide, ifosfamide, vincristine, and methotrexate, are considered as first-line therapies for bone tumors [7]. However, the mineralized matrix of bone impedes the distribution of anticancer agents, resulting in insufficient therapeutic effects and drug resistance [8]. Furthermore, the low blood supply to bone contributes to the low therapeutic effects of the agents.

1.2. Nano delivery platforms to enhance the bone tumor accumulation

To enhance the tumor accumulation and tumor microenvironment-induced resistance, various functionalized nanoplatforms have been designed to improve the accumulation of anticancer drugs in bone tumor tissues [9-12]. Most of the engineered particles were composed of various functionalized polymers and inorganic materials, functionalized with bone-homing or tumor microenvironment-responsive molecules. The bone homing particles have a strong affinity to the bone matrix, leading to the accumulation in bone tumors. Meanwhile, microenvironment-responsive particles specifically release the drugs in the bone tumor microenvironment. Among these, bisphosphonate-decorated nanoparticles have been extensively studied because of their high affinity for the hydroxyapatite matrix [13].

These nanoplatforms are generally designed to have a particle size large enough to take advantage of the wide inter-endothelial gaps in tumor vasculature, which is well-understood as the enhanced permeability and retention effect [14]. However, concerns remain that large nanoparticles utilizing the size-exclusion mechanism may cause unwanted long-term accumulation of drugs in the mononuclear phagocyte system (MPS) [15]. It was hypothesized that a nanocluster (NC) system that can spontaneously disassemble into smaller units might avoid or rapidly escape from non-

specific MPS disposition, thereby yielding an improved tumor-to-liver accumulation ratio. Considering that soluble protein can reversibly self-assemble into various nanoscale supramolecular structures, protein nanoclusters with bisphosphonate moieties were designed [16].

1.3. Bisphosphonate as a targeting moiety for hydroxyapatites in the bone tumor microenvironment

Bisphosphonates are used in the management of patients with various bone-related disorders, including osteoporosis, metastatic bone tumors, and Paget's disease [17]. The highly selective uptake and binding to bone minerals are determined by their unique structure of two phosphonate groups that form ionic interactions with calcium in bone. Among many bisphosphonates, the most effective structures are the two phosphonate groups attached to a central carbon and substitution with a hydroxyl or amino group that provides tridentate binding. They suppress the function of osteoclasts and increase skeletal retention. In bone tumor management, they are commonly used as adjuvant therapy to relieve the pain.

1.4. Limitations of previous nano delivery platforms for bone tumor treatment

The bone-targeting particles commonly had a rigid structure with a mean diameter of 100 – 300 nm, thereby the particles increase the blood

circulation and tumor distribution by EPR effect. Functional moieties of the particles could work after the size-dependent distribution. However, the effectiveness of EPR effect remains uncertain. Many researchers have strongly claimed that the inter-endothelial gaps rarely contributed to the tumor distribution of nanoparticles [18]. This low tumor distribution efficiency is highly disadvantageous to the bone tumor as the blood flow to a bone is quite low, compared to other organs. Thus, EPR-based nanoparticles would not be suitable for bone tumor treatment.

Another limitation is that the particles with nanometers could be entrapped by innate immune system, causing unwanted long-term accumulation of drugs. The unintended accumulation leads to distribution to normal organs and impedes the tumor distribution. Many factors are considered as causes of the problem, including size, surface charge, and shape of particles [15]. Among them, the most important characteristic is considered to be the particle size. Thus, the unwanted distribution might be alleviated by making particle size smaller.

1.5. Albumin-based drug delivery system

Albumin has been extensively investigated as a carrier material for tumor-targeted drug delivery, including metastatic breast cancer, non-small-cell lung cancer (NSCLC), and metastatic pancreatic cancer [19-21]. The nanocarriers are composed of drug-loaded modified albumin with a particle

size of 100 – 200 nm. The drug-loaded albumin can bind to various albumin receptors that overexpressed in tumor vasculature and be transported to the tumor [22,23]. Thus, their tumor distribution was dependent on the receptor-mediated transcytosis, not on the inter-endothelial gaps. As the receptor-mediated transcytosis was already proven to be effective in tumor distribution [18], the albumin-based nanocarriers would be more effective than conventional nanoparticles that rely on the size-dependent distribution.

Albumin-based nanocarriers are advantageous for tumor uptake. Tumor cells express many albumin receptors on their surface and engulf the drug-loaded albumin as an amino acid source for growth. The engulfed albumin was fully digested, during which the loaded drugs are released, exhibiting the antitumor effect. These receptor-mediated transcytosis and endocytosis facilitate the tumor uptake and distribution. Moreover, albumin can bind with osteonectin, a bone protein overexpressed in various human cancers, which is also known as secreted protein acidic and rich in cysteine (SPARC). Notably, osteonectin plays a pivotal role in tumor growth by promoting angiogenesis, cancer cell invasion, and bone migration [24,25]. In this regard, albumin was selected as the core material for fabricating bone tumor-directed drug delivery systems.

The objective of this study was to develop a novel self-assembled DOX-loaded alendronate-decorated human serum albumin nanoclusters (NCs) was developed for efficient bone tumor-targeted therapy (Fig. 1). The NC fabrication was conducted *via* ball-milling technology (BMT), a newly

developed method wherein the native conformation of albumin was preserved. The targeting ability to the bone tumor was evaluated in a hydroxyapatite bead-incorporated cell culture and mouse models, representing the bone tumor microenvironment. The therapeutic efficacy and systemic toxicity of the NCs were also investigated in the developed mouse model.

2. Materials and Method

2.1. Materials

Human serum albumin (HSA), 1-ethyl-3-(3-dimethylaminopropyl) carbodiimide (EDC), *N*-hydroxysuccinimide (NHS), triethylamine (TEA), and hydroxyapatite (5 μm, surface area ≥ 100 m^2/g) were purchased from Sigma-Aldrich (St. Louis, MO, USA). Alendronate sodium trihydrate (AD) and glutaraldehyde were purchased from Tokyo Chemical Industry Co., Ltd. (Tokyo, Japan). DOX hydrochloride (DOX HCl) was obtained from LC Laboratories (Woburn, MA, USA).

2.2. Synthesis of HSA-AD

HSA-AD conjugates were synthesized *via* the EDC/NHS coupling reaction. HSA (100 mg) was dissolved in double deionized water (DDW; 20 mL) at 25 °C. EDC (14.42 mg) and NHS (8.67 mg) were added to the

solution, and the mixture was stirred for 30 min to activate the carboxylic acids of HSA. Subsequently, AD (10 mg) and TEA (20.48 μL) were added to the mixture and stirred for 24 h. The product was dialyzed (molecular weight cut-off: 12–14 kDa) against water for 24 h and further purified using a desalting column (PD-10; GE Healthcare, Chicago, IL, USA) to remove the unreacted AD. After lyophilization, the HSA-AD powder was stored at -70 °C until use. The conjugation of AD to HSA was verified in terms of the increase in molecular weight and the presence of phosphorus in HSA-AD. The molecular weights of HSA and HSA-AD were determined using matrix-assisted laser desorption ionization-time of flight (MALDI-TOF) mass spectrometry (Voyager DE-STR; Applied Biosystems, Foster City, CA, USA). AD, HSA, and HSA-AD were analyzed using phosphorus-31 nuclear magnetic resonance (^{31}P-NMR; AvanceIII-500; Bruker, Billerica, MA, USA). All NMR samples were prepared using deuterium oxide (D_2O) solution.

2.3. Fabrication of DOX-loaded albumin nanoclusters (NCs)

DOX base was prepared from DOX HCl using a liquid-liquid extraction method. Briefly, DOX HCl (60 mg), dissolved in DDW (10 mL), was mixed vigorously with chloroform (40 mL) containing TEA (50 μL) in a separatory funnel. The chloroform phase was collected and completely evaporated using a rotary evaporator. The precipitated DOX base was

dissolved in a minimal amount of DMSO and lyophilized. The ball-milling technology-assisted fabrication of HSA/DOX and HSA-AD/DOX NCs was performed using a Tissuelyser LT (QIAGEN, Hilden, Germany). DOX base (4 mg) was dispersed in DMSO (4.75 μL) *via* sonication for 10 min and was subsequently vortex-mixed with phosphate-buffered saline (PBS; 42.5 μL). HSA or HSA-AD (20 mg) was added to the suspension with a stainless-steel bead (diameter: 5 mm; QIAGEN) and milled at 50 rpm for 3 min. After milling, the resulting suspension was lyophilized to remove the solvent. The lyophilized composite was dispersed with DDW *via* gentle vortex mixing. The suspension was centrifuged at 16,000 × *g* for 1 min and filtered with a syringe filter (pore size: 0.2 μm) to remove precipitates, mostly unbound DOX. The drug content was quantified using a UV-Vis spectrophotometer (EMax Precision Microplate Reader; Molecular Devices, San Jose, CA, USA), wherein the NC suspension was diluted with a 9.5% DMSO solution (dilution factor: 20) and analyzed at a wavelength of 470 nm. Meanwhile, as control groups, conventional albumin nanoparticles (NPs) were prepared with HSA and HSA-AD using a solvent displacement method. Briefly, HSA or HSA-AD (50 mg) was dissolved in DW (2 mL) and ethanol (4 mL for HSA and 1 mL for HSA-AD) was added dropwise to the solution while stirring. Glutaraldehyde (10 μL) was added to the suspension and stirred for 3 h, followed by centrifugation at 16,000 × *g* for 5 min. The pellet was resuspended in DDW to generate HSA and HSA-AD NPs.

2.4. Characterization

Particle size, polydispersity index, and zeta potential values were measured using electrophoretic light scattering (ELS-Z; Otsuka Electronics, Osaka, Japan). Morphological observations were performed using field-emission transmission electron microscopy with energy dispersive spectroscopy (JEM-F200; JEOL, Tokyo, Japan). Samples were prepared on a copper grid with a carbon film, and atomic analysis was conducted for three different atoms, including carbon, oxygen, and phosphorus. Circular dichroism spectra were recorded in the wavelength range of 180–260 nm using a Chirascan Plus spectrometer (Applied Photophysics, Surrey, UK). The analytical samples were prepared in DDW at a concentration of 0.1 mg/mL. The denatured HSA sample was prepared by heating the HSA solution to 80 °C. The contents of the secondary structure motifs were calculated using the CDNN software. The colloidal stability of the developed NCs was tested in PBS and fetal bovine serum (FBS; ATCC, Manassas, VA, USA) at room temperature for 7 days, to assess the changes in particle size and drug content. The mean diameter and PDI were measured using an ELS-Z instrument (Otsuka Electronics). The drug content was quantified using a UV-Vis spectrophotometer (EMax Precision Microplate Reader; Molecular Devices) after removing the precipitated NCs by centrifugation at 1,200 × *g* for 3 min. The disassembly of the NCs was

evaluated by measuring their mean diameters after dilution with 50% FBS at various dilution factors.

2.5. *In vitro* drug release test

In vitro DOX release patterns from the NCs were evaluated using mini-GeBAflex tubes (molecular weight cut-off: 14 kDa; Gene Bio-Application Ltd, Yavne, Israel). Each tube loaded with NC suspension (100 μL) was immersed in PBS at various pH values (30 mL; pH 5.5, 6.8, and 7.4, adjusted with phosphoric acid) and incubated in shaking water bath at 37 °C (50 rpm). Aliquots of the release media were collected at 0.5, 1, 2, 4, 7, 10, 24, 48, 72, and 96 h and the same volume of fresh medium was replenished at each time point. The DOX concentration of each sample was analyzed using high-performance liquid chromatography system equipped with a separation module (Waters e2695; Waters Co., Milford, MA, USA), a fluorescence detector (Waters 2475; Waters Co.), and a reverse phase C18 column (Xbridge RP18, 250 × 4.6 mm, 5 μm; Waters Co.). The mobile phase consisted of 10 mM potassium phosphate buffer (pH 2.5, adjusted with phosphoric acid) and acetonitrile with 0.1% TEA (71:29, v/v). The flow rate and injection volume were set at 1.0 mL/min and 20 μL, respectively. The eluent was monitored at excitation and emission wavelengths of 470 and 565 nm, respectively. The cumulative drug release

(F; %) against time (t) profile was fitted using five mathematical models, the equations of which are as follows:

First-order model: $F = F_{max} \times (1 - e^{-kt})$

Higuchi model: $F = k_H \times t^{0.5}$

Baker-Lonsdale model: $\frac{3}{2}\left[1 - \left(1 - \frac{F}{100}\right)^{\frac{2}{3}}\right] - \frac{F}{100} = k_{BL} \times \mathrm{t}$

Korsmeyer-Peppas model: $F = k_{KP} \times \mathrm{t}^{n}$

Peppas-Sahlin model: $F = k_1 \times t^{m} + k_2 \times t^{2m}$

where F_{max} is the maximum cumulative release, and k, k_H, k_{BL}, k_{KP}, k_1, and k_2 are the release rate constants of the corresponding models.

2.6. Cell culture conditions

Human umbilical vein endothelial cells (HUVECs) with passage number 2 were purchased from PromoCell (Heidelberg, Germany) and cultured in endothelial cell growth medium 2 (PromoCell) containing 4% (v/v) supplement Mix (PromoCell) and 1% (v/v) penicillin/streptomycin (PS; 100 U/mL and 0.1 mg/mL, respectively; Welgene, Gyeongsan, Republic of Korea). HOS/MNNG cells, a human osteosarcoma cell line, of passage number 7 were obtained from ATCC and cultured in Eagle's minimum essential medium (EMEM; ATCC) supplemented with 10% FBS

(ATCC) and 1% PS (Welgene). Both types of cells were incubated at 37 °C in a 5% CO_2 atmosphere.

2.7. Confocal Laser Scanning Microscope (CLSM) analysis

A confocal laser scanning microscope (CLSM; TCS8; Leica Microsystems, Wetzlar, Germany) was used to visualize the cellular distribution of DOX. HUVECs (3×10^5 cells) were seeded onto a 4-chamber slide (SPL Life Sciences, Pocheon, Republic of Korea) and treated with DOX solution or DOX-loaded NC suspension at a DOX concentration of 20 μg/mL. To verify the caveolae-mediated uptake of HSA-AD/DOX, methyl-β-cyclodextrin (Sigma-Aldrich) was pre-incubated for 15 min as a caveolae-mediated receptor inhibitor. After 1 h of incubation, the cells were washed twice with PBS and fixed in 4% (v/v) formaldehyde solution for 10 min. Cell nuclei were labeled with 4,6-diamidino-2-phenylindole (DAPI; Vector Laboratories, Burlingame, CA, USA). HOS/MNNG cells (3×10^5 cells) were seeded onto a hydroxyapatite-coated cell culture slide, which was prepared in-house; hydroxyapatite beads (1 mg) and collagen solution (10 μg; Corning Inc., Corning, NY, USA) were mixed and dispersed onto a cell culture slide (2 cm^2) and dried at 25 ℃ for 24 h to obtain the hydroxyapatite-coated slide. DOX solution or DOX-loaded NC suspension was treated at a DOX concentration of 20 μg/mL and incubated for 1 h. To verify receptor-mediated tumor uptake, free HSA was used as a competitive

inhibitor. The slides were washed and fixed in the same manner as the HUVECs. Z-stack observations were performed at a depth of 20 μm.

2.8. Flow cytometry analysis

For flow cytometric analysis, HOS/MNNG cells (1.5×10^5 cells) and HUVECs (1.5×10^5 cells) were cultured in a 6-well plate. DOX solution or DOX-loaded NCs (5 μg/mL as DOX) were incubated for 3 and 6 h with HUVECs, and 1 and 3 h with HOS/MNNG cells. The inhibitors were treated at the same concentrations as those used in the CLSM studies. The cells were rinsed twice with PBS, trypsinized from the plate, and centrifuged at 200 × *g* for 5 min. The cell pellets were resuspended in PBS with 2% FBS and analyzed using FACS Calibur (BD Biosciences, San Jose, CA, USA).

2.9. Transwell study

For the transwell assay, HUVECs (1×10^5 cells) were cultured on a 0.4 μm pore membrane filter (1.12 cm^2; Corning Inc., Corning, NY, USA) until trans epithelial electrical resistance (TEER) values reached 150 – 160 ohms. Free HSA was used as a positive control, and MBC (2 mM) and chlorpromazine hydrochloride (CPZ; 50 μM; Sigma-Aldrich, St. Louis, MO, USA) were co-treated with HSA-AD/DOX. All groups were incubated in a transport medium (PBS) for 2 h. The amount of transported HSA was

measured using BCA assay kit (Thermo Fisher Scientific, Waltham, MA, USA).

2.10. *In vitro* antitumor efficacy and cytotoxicity

The *in vitro* anticancer activity of the NCs was assessed using the 3-(4,5-dimethyl-2-yl)-5-(3-carboxymethoxyphenyl)-2-(4-sulfophenyl)-2*H*-tetrazolium (MTS) assay. HOS/MNNG cells were seeded onto 96-well plates and incubated for 72 h with DOX solution or DOX-loaded NCs at various DOX concentrations (0.1, 0.2, 0.5, 1, 2, and 3 μM). After removing the treatment solution, MTS reagent (CellTiter 96 AQueous One Solution Reagent; Promega, Madison, WI, USA) was added to the cells and incubated for 4 h at 37 °C. Absorbance was then measured at a wavelength of 490 nm using a UV-Vis spectrophotometer (EMax Precision Microplate Reader; Molecular Devices). IC_{50} values were calculated using Prism 8.0.2 (GraphPad Software, San Diego, CA, USA). The cytotoxicity of blank HSA and HSA-AD was also evaluated using the same method described above, where each protein was treated with various concentrations (5, 10, 20, 50, 100, 200, 500, 1000, 2000, and 5000 μg/mL).

2.11. Affinity to hydroxyapatite

The affinity of HSA-AD/DOX to hydroxyapatite was assessed in terms of the amount of DOX adsorbed onto hydroxyapatite. HSA/DOX or

HSA-AD/DOX (50 μg/mL as DOX) were vortex-mixed with hydroxyapatite beads (10 mg) for 1 min, followed by centrifugation at 16,000 × *g* for 1 min. The supernatant was analyzed using a UV-Vis spectrophotometer (EMax Precision Microplate Reader; Molecular Devices). The adsorbed amount of DOX was calculated as follows: (DOX concentration before centrifugation – DOX concentration of supernatant) × volume. In addition, the adsorption of NCs to hydroxyapatite was also investigated using flow cytometry, wherein HSA/DOX or HSA-AD/DOX (50 μg/mL as DOX) were incubated with hydroxyapatite beads (10 mg) under vigorous vortex-mixing for 1 min. The beads were sorted and relatively quantified using FACS Calibur (BD Biosciences) in the fluorescence-2 channel for the detection of DOX signals.

2.12. Animal models

Nude Balb/c mice (female; 5-weeks-old; Nara Biotech, Seoul, Republic of Korea) were reared in a light-controlled room at a temperature of 22 ± 2 °C and relative humidity of 55 ± 5% (Animal Center for Pharmaceutical Research, College of Pharmacy, Seoul National University, Seoul, Republic of Korea), to establish heterotopic and orthotopic bone tumor xenograft models. The experimental protocol (SNU-210121-10-1) for the animal study was approved by the Animal Care and Use Committee of Seoul National University. The heterotopic bone-tumor model was prepared

through subcutaneous inoculation of an osteosarcoma cell suspension with bone matrix components in the lower right flank of the mice. The suspension consisted of HOS/MNNG cells (5×10^6 cells) and hydroxyapatite beads dispersed in a mixture of culture media and Matrigel (*i.e.*, collagen) (1:1, v/v; total volume of 0.1 mL). Hydroxyapatite beads (4 mg) were washed with ethanol and dried overnight to avoid microbial contamination. The orthotopic model was prepared through intratibial injection of HOS/MNNG cell suspension (5×10^6 cells in 0.1 mL of culture media) on the right leg of the mice.

2.13. Near-infrared fluorescence imaging

Near-infrared fluorescence (NIRF) imaging was conducted in both heterotopic and orthotopic models. Cy5.5, an imaging dye, was conjugated to investigate the behavior of the developed NCs. Briefly, Cy5.5-NHS ester (150 μg; Flamma® 675 NHS ester; BioActs, Incheon, Republic of Korea) was added to HSA or HSA-AD (25 mg) dissolved in DDW (1 mL), which was then stirred for 4 h at 25 ℃ and purified using a PD-10 desalting column (Cytiva, Marlborough, MA, USA). DOX-loaded NCs were prepared with Cy5.5-labeled HSA and HSA-AD according to the same method used to fabricate HSA/DOX and HSA-AD/DOX. The resulting NIRF dye-tagged NCs were injected into the tail vein of the mice at a Cy5.5 dose of 0.12 mg/kg after the tumor volume of the heterotopic model reached 150–200

mm^3, which was calculated as follows: 0.5 × longest diameter × (shortest diameter)^2. In the orthotopic model, where the tumor size could not be measured, the NCs were administered at a Cy5.5 dose of 0.035 mg/kg 3 weeks after the inoculation. Whole-body scans were performed using VISQUE InVivo Smart (Vieworks, Anyang, Korea) equipped with the CleVue™ software (Vieworks) at 0, 1, 3, 5, 7, 9, 11, and 24 h post-injection for the heterotopic model, and 0, 3, 5, 7, 9, and 24 h for the orthotopic model. The mice were euthanized at 24 h after injection, and their tumors and major organs, including the heart, liver, kidney, lung, spleen, and lung were dissected for *ex vivo* imaging. For histological analysis, the tumors were sectioned, stained with alizarin red S (Sigma-Aldrich), and observed using CLSM (TCS8; Leica Microsystems). The fluorescence profile of Cy5.5-labeled HSA or HSA-AD NPs (*i.e.*, conventional albumin nanoplatforms) was also investigated using an orthotopic xenograft model. The Cy5.5-labeled NPs were prepared by adding Cy5.5-NHS in the final step of fabrication. The NPs were injected into the tail vein of the mice at a Cy5.5 dose of 0.035 mg/kg. Fluorescence images were obtained at 0, 1, 3, 8, and 24 h, after which the tumor-bearing mice were euthanized and their major organs (heart, liver, kidney, lung, and spleen), including both legs, were dissected to analyze the biodistribution of the NPs.

2.14. *In vivo* antitumor efficacy

An *in vivo* antitumor efficacy test was performed in a hydroxyapatite-containing tumor model. Tumor volume (mm^3) and body weight (g) were monitored daily after inoculation. The experimental groups were as follows: no intervention, DOX solution, HSA/DOX, and HSA-AD/DOX. The formulations were injected intravenously at a DOX dose of 5 mg/kg on days 6, 8, 10, 13, and 15. On day 16, the experiment was terminated, and the tumors of each mouse were excised and weighed. The major organs, including the heart, liver, kidney, and spleen, were also examined for histological changes. The terminal deoxynucleotidyl transferase dUTP nick-end labeling (TUNEL) assay was performed on tumor tissues. The organs were stained with hematoxylin and eosin (H&E).

2.15. Antibody microarray analysis

Protein expression patterns of tumors were investigated using Signaling Explorer Antibody Array Kit (Fullmoon Biosystem, Inc.; Sunnyvale, CA, USA). To prepare the samples, the DOX solution or NCs were intravenously injected (5 mg/kg as DOX) daily for consecutive 3 days to the hydroxyapatite-containing xenografted mice after the tumor volume reaches 100–120 mm^3. The untreated group was used as a control for fold change analysis. On the day after the final treatment, each tumor was dissected, and the soluble proteome was extracted with protein extraction

buffer (Fullmoon biosystems) containing 1% protease inhibitor cocktail (Sigma-Aldrich), lysis beads (Fullmoon biosystems), and 1% phosphatase inhibitor cocktail (Sigma-Aldrich). The extracted solution was purified using a gel matrix column included in the kit. The column was vortex-mixed for 5 s, hydrated for 60 min at room temperature, and centrifuged at 750 × *g* for 2 min. Next, the column was placed into a collection tube, to which an aliquot (100 μL) of the protein sample was loaded. The column was centrifuged at 750 × *g* for another 2 min. The concentration of purified samples was measured with a BCA protein assay kit (Pierce, Rockford, IL, USA) using NanoPhotometer^{TM} (Implen, Munich, Germany). The purity of the samples was evaluated based on UV spectra. The prepared samples were subjected to antibody microarray assay according to the manufacturer's protocol. Then, the array slides were scanned using GenePix 4100A scanner (Molecular Devices, San Jose, CA, USA) at 10 μm resolution. Scanned images were quantified with GenePix 7.0 Software (Molecular Devices). All protein information was annotated using the UniProt database (UniProt Consortium). Data mining and graphic visualization were performed using ExDEGA (Ebiogen Inc., Seoul, Korea). Gene set enrichment analysis (GSEA) was conducted using GSEA 4.1.0 software (Broad Institute, Inc., MA, USA).

2.16. Statistical analysis

All experiments were performed at least thrice, and data are presented as mean ± standard deviation (SD). Statistical analyses were performed using analysis of variance (ANOVA) with Tukey's multiple comparisons test or two-tailed *t*-test. Statistical significance was set at $p < 0.05$.

3. Results and Discussion

3.1. Synthesis of HSA-AD

To enhance the targeting ability of albumin, bisphosphonate was decorated *via* the amide bond formation between the activated carboxylic acid groups of human serum albumin (HSA) and primary amine of alendronate (AD) [26-28]. The successful synthesis of the HSA-AD conjugate was verified *via* matrix-assisted laser desorption ionization-time-of-flight (MALDI-TOF) mass spectrometry (Fig. 2). The use of HSA-AD led to an increased average mass-to-charge ratio (*m/z*) of 67,468 compared to that obtained with the unmodified HSA (*m/z* 66,500), indicating that the average number of conjugated AD molecules per HSA was calculated as 4.20. Moreover, phosphorus-31 nuclear magnetic resonance analysis (^{31}P-NMR) of HSA-AD revealed the presence of phosphorus displaying a peak at 15.65 ppm (Fig. 3). A similar pattern was observed in the spectrum of free AD (18.34 ppm), whereas unmodified HSA exhibited no peak within the range of -200 to 200 ppm. The phosphorus in HSA-AD confirmed the conjugation of AD.

3.2. Ball-milling technology (BMT) for fabricating the NCs

Various conventional methodologies for fabricating albumin nanoplatforms have been described in some literature, including solvent displacement, emulsification, and thermal gelation [29-31]. However, these

procedures caused denaturation and irreversible aggregation of albumin molecules due to the involvement of organic solvents, chemical crosslinkers, or high temperatures. In our preliminary study, conventional albumin nanoplatforms fabricated *via* solvent displacement methods exhibited an unfavorable biodistribution profile, and the bone tumor-to-liver accumulation ratio was as low as 0.52, even with surface decoration with bisphosphonate moieties (Fig. 4).

Thus, to address this issue, a new fabrication method based on ball milling was developed, which requires only a minimal amount of solvent and physical impact (Table 1). In this study, doxorubicin (DOX) was used as a model drug. Briefly, DOX and HSA were dispersed in the solvent using a rapidly moving stainless steel bead. This process can accelerate the mechanochemical interactions between drugs and proteins [22,23], whereby the DOX-loaded albumins were self-assembled to nanoclusters. The ball-milled mixture was then lyophilized to remove the organic solvent, reconstituted with double-deionized water (DDW), and filtered to eliminate unloaded DOX. The obtained NCs, namely HSA/DOX and HSA-AD/DOX, exhibited no precipitation even at high DOX concentrations (~ 1 mM), whereas free DOX was precipitated in DDW because of its low solubility (~ 1.8 μM) (Fig. 5).

The ball-milling process provides the physical energy that can promote the adsorption of DOX onto the protein surface and may induce the self-assembly of the resulting protein/DOX complex into NCs [34], which

resembles the high-pressure homogenization step in the nanoparticle albumin-bound (nab®) technology [35]. Notably, only 3 min of the ball-milling process considerably improved the drug adsorption of HSA/DOX and HSA-AD/DOX (6.13 ± 0.20% and 6.11 ± 0.29%, respectively) compared to the vigorous vortex-mixing for 12 h (0.397 ± 0.003% and 0.309 ± 0.003%, respectively) (Table 2).

3.3. Physicochemical properties

The fabricated HSA/DOX and HSA-AD/DOX showed a similar mean diameter of 163 ± 3 nm and 161 ± 4 nm, respectively (Table 3). Both NCs showed unimodal distribution with narrow PDI values (Fig. 6 and Table 3). In contrast, the zeta potential value of HSA-AD/DOX (-42.1 ± 9.6 mV) was more negative than that of HSA/DOX (-21.1 ± 1.5 mV), which might be attributed to the highly negative surface of phosphate groups of the AD moieties. Thus, the AD conjugation induced greater negative surface charge of albumin. The highly negative surface charge might be advantageous to the stability of the NCs.

3.4. Microscopic and atomic analyses

Fig. 7 indicated the Transmission electron microscopy (TEM) images of HSA/DOX and HSA-AD/DOX to visualize the surface morphology. Both NCs showed sphere-shaped nanoclusters, of which

diameters were consistent with the values of DLS (Fig. 6). The TEM images verified the successful fabrication of NCs. In addition, transmission electron microscopy-energy dispersive spectroscopy (TEM-EDS) analysis revealed that HSA-AD/DOX possessed phosphorus atoms on its surface, indicating that the AD moieties were exposed on the surface the NCs (Fig. 8).

3.5. Investigation of secondary structures

Circular dichroism (CD) spectroscopy was performed to investigate the secondary structure of the NCs (Fig. 9). In this investigation, native HSA and heated HSA were used as positive and negative controls. The HSA-AD (*i.e.,* HSA-AD without DOX), HSA/DOX, and HSA-AD/DOX exhibited the characteristic mean residue ellipticity at 190 nm (positive), 208 nm (negative), and 222 nm (negative), indicating that only a negligible conformational disruption (slight reduction in α-helix content less than 10%) occurred during AD conjugation or DOX loading *via* BMT (Table 4). However, albumin nanoplatforms prepared using the conventional desolvation method showed drastic changes in their secondary structures. Compared to that of the native HSA, the α-helix content of these nanoparticle conjugates significantly decreased by more than 45%, displaying a pattern similar to that of heat-denatured HSA.

3.6. Stability test

Although negligible conformational changes were observed after the fabrication of NCs, it was essential to investigate whether AD conjugation and/or DOX adsorption compromises the colloidal stability of NCs. Fig. 10 shows that the developed NCs maintained their initial size with a PDI value of approximately 0.3, even after seven days of incubation in a high ionic strength buffer or serum at room temperature, implying that their colloidal stability was sufficient for intravenous administration. Interestingly, however, both NCs were spontaneously disassembled into smaller units upon dilution, showing concentration-dependent reduction in the mean diameter (Fig. 11).

3.7. *In vitro* drug release test

The DOX release patterns from the NCs were monitored under different pH conditions, and each profile was fitted using various mathematical models (Fig. 12 and Table 5). Interestingly, the first-order model presented the highest correlation coefficient compared to the others, which implies that the DOX release from NCs may follow the drug-protein dissociation model [36]. Moreover, the maximum cumulative release of the NCs increased as the pH of the media decreased, which can be explained by the increased solubility of DOX resulting in the reduced interactions between the drug and the NCs [37]. Considering that the pH values of 5.5,

6.8, and 7.4 correspond to the pH values of the endolysosomal compartments, the tumor microenvironment, and normal tissues (or plasma), respectively, the higher drug release at acidic pH values may result in enhanced drug exposure in tumor tissues compared to that in normal organs [38].

3.8. *In vitro* cellular uptake and hydroxyapatite-binding ability test using bone tumor microenvironment-mimicking cell culture model.

The cellular uptake mechanism of the bisphosphonate-conjugated albumin NCs was investigated in a 2D bone tumor microenvironment-mimicking cell culture model, where HOS/MNNG cells and hydroxyapatite beads/collagen were co-cultured. (Fig. 13). HOS/MNNG (human osteosarcoma) cells were selected due to their propensities for high invasion, migration, and proliferation, as well as tumorigenicity and colony-forming ability [39]. Confocal microscopy observation revealed that the use of HSA-AD/DOX led to enhanced DOX uptake by cells compared to free DOX solution and HSA/DOX (Fig. 14). However, the DOX signal decreased when free HSA was used as a competitive inhibitor, indicating that the albumin uptake mechanism, including receptor-mediated endocytosis, contributes in part to the uptake of HSA-AD/DOX by HOS/MNNG cells [39-42]. Thus, the passive diffusion mechanism of DOX

solution into the cells was changed to the receptor-mediated endocytosis by adsorption on the albumin. HSA-AD/DOX also displayed a higher affinity to the hydroxyapatite beads/collagen matrix than HSA/DOX, which can be attributed to the ionic interactions between AD and hydroxyapatite [43]. Although this cell culture model could not fully reflect the tumor microenvironment, such as nutrients, the concentration of hydroxyapatites, and heterogeneity in the extracellular matrix, it might be useful for observing the behavior of the modified NCs.

The uptake mechanism was further confirmed by quantifying the fluorescence intensity of DOX using flow cytometry (Fig. 15). Similar to the microscopy data, HSA-AD/DOX exhibited improved uptake efficiency in both HOS/MNNG (1.59-fold at 3 h) compared to the free DOX solution. In addition, the DOX uptake of HSA-AD/DOX decreased significantly in the presence of inhibitors (free HSA). Although the decreased intensity might not be caused only by the competitive inhibition of free HSA considering the binding affinity to albumin, the time-dependent decrease of intensity may indicate the albumin receptor-mediated endocytosis of the NCs.

The binding affinity of HSA-AD/DOX to hydroxyapatite was confirmed using flow cytometry, wherein hydroxyapatite beads were treated with each formulation, and the DOX fluorescence signals emitted from the beads were measured (Fig. 16). HSA-AD/DOX-treated beads exhibited a significantly higher fluorescence intensity than the HSA/DOX (2.41-fold)

and free DOX (3.37-fold) groups. Similar results were observed in the drug adsorption study using UV-Vis spectrophotometry, where the slope of the adsorbed drug amount versus concentration curve was 5.04-fold steeper in HSA-AD/DOX than HSA/DOX (Fig. 17). These findings suggest that AD conjugation significantly improves the binding affinity of NCs to the hydroxyapatite matrix.

3.9. *In vitro* cellular uptake test using HUVECs.

A cellular uptake study was also performed in human umbilical vein endothelial cells (HUVECs) to verify the transcytosis mechanism of albumin NCs in the tumor vasculature [22,23]. HUVECs were selected given their gp60-rich characteristics [44], and methyl-β-cyclodextrin (MBC) was used as an inhibitor of caveolae-mediated transcytosis [22,23]. As shown in Fig. 18, both albumin NCs exhibited more efficient cellular uptake than the DOX solution. Notably, MBC inhibited the entry of HSA-AD/DOX into HUVECs, suggesting the involvement of caveolae-mediated transcytosis in its cellular uptake.

The uptake mechanism was further confirmed by quantifying the fluorescence intensity of DOX using flow cytometry (Fig. 19). Similar to the microscopy data, HSA-AD/DOX exhibited improved uptake efficiency in HUVECs (1.50-fold at 6 h) compared to the free DOX solution. In

addition, the DOX uptake of HSA-AD/DOX decreased significantly in the presence of inhibitors.

3.10. Transwell study

Transcytosis of the NCs through HUVECs was assessed by Transwell assay system (Fig. 20). Free HSA was used as a positive control, and MBC and chlorpromazine HCl (CPZ) were used as inhibitors for caveolae- and clathrin-mediated transcytosis, respectively [45]. The percent transported amount of HSA at 2 h reached 49.3 ± 2.9% and 50.9 ± 5.4% of the initial amount in HSA/DOX and HSA-AD/DOX groups, respectively, which were slightly lower than that of the control free HSA (64.9 ± 2.0% at 2 h). The increased particle size by self-assembly seemed to reduce the transport of HSA compared to free HSA, whereas the conjugation of AD on HSA did not affect its transport. Of note, MBC treatment significantly decreased the amount of HSA transported (0.43-fold at 2 h), while CPZ treatment showed an insignificant inhibitory effect on the transport (0.90-fold at 2 h). The strong inhibitory effect of MBC suggests that the interaction with caveolae-mediated albumin receptors could be the major pathway for the transcytosis of HSA-AD/DOX.

3.11. *In vitro* antitumor efficacy and cytotoxicity tests

The cytotoxicity of DOX-loaded NCs against HOS/MNNG cells was investigated using a tetrazolium-based cell viability assay (Fig. 21). Both HSA/DOX and HSA-AD/DOX suppressed the proliferation of HOS/MNNG in a dose-dependent manner, with IC_{50} values of 1.038 ± 0.044 μM and 0.975 ± 0.076 μM, respectively (Fig. 21a). These values were significantly lower than those of the DOX solution (1.666 ± 0.148 μM), which can be explained by the improved cellular uptake efficiency of the developed NCs. HSA-AD exhibited no significant cytotoxicity even at a concentration higher than the physiological HSA level, suggesting its high biocompatibility (Fig. 21b).

3.12. Near-infrared fluorescence (NIRF) imaging in a bone tumor-mimicking xenografted mouse model.

The biodistribution of NCs was evaluated using near-infrared fluorescence (NIRF) imaging after intravenous administration. In this investigation, a new bone tumor xenograft mouse model was developed by co-culturing HOS/MNNG cells and hydroxyapatite beads (Fig. 22). In this model, the hydroxyapatite content of xenografted tumors was estimated to be 2.7–4.0% (w/w), of which the degree was highly consistent with the calcification of mature bone tumors (3.91 ± 0.35%, w/w) [46]. To validate the model, the established tumor was sliced and stained with H&E and

alizarin red S (Fig. 23). The H&E and alizarin red S images indicate the tumor cells and hydroxyapatites, respectively. The images indicate that hydroxyapatites were located in the extracellular matrix and cancer cells grew well in the xenografted tumor, suggesting the establishment of bone tumor-mimicking environments.

To monitor the behaviors of NCs in the mouse model, Cy5.5-labeled HSA/DOX and HSA-AD/DOX were injected intravenously, and whole-body was scanned for a 24-h period (Fig. 24a). Interestingly, both HSA/DOX and HSA-AD/DOX gradually accumulated in the tumor region for up to 9 h and were retained until the experiment ended. However, the average radiant efficiency versus time profile of the tumor region clearly showed that HSA-AD/DOX exhibited significantly higher tumor deposition than HSA/DOX (Fig. 24b). The *ex vivo* imaging data showed the biodistribution of the NCs and significantly greater tumor distribution (Fig. 25a). HSA-AD/DOX exhibited the significantly increased average radiant efficiency value than HSA/DOX, confirming a higher tumor distribution (Fig. 25b). As demonstrated by in Fig. 16 and 17, the enhanced tumor distribution can be explained by a higher affinity to hydroxyapatites.

3.13. Histological analysis of the dissected tumors

Histological analysis of the tumor tissue was also performed to investigate the localization of HSA-AD/DOX in the tumor (Fig. 26) [47].

Notably, HSA-AD/DOX showed strong co-localization with alizarin red S, indicating that bisphosphonate decoration can be a valid strategy for targeting the bone tumor microenvironment with calcification. This phenomenon was also observed through NIRF imaging of excised tumors on a macroscopic scale (Fig. 27). As the tumor outgrew the inoculation area, a part of the tumor containing hydroxyapatite beads was separated; HSA-AD/DOX accumulated in this part of the tumor to a greater extent than in the other part, which corresponds well with the above-obtained histological data.

3.14. Near-infrared fluorescence (NIRF) imaging in an orthotopic mouse model.

The NIRF imaging study was also performed in an orthotopic xenograft model, in which bone tumors were developed after intratibial injection of HOS/MNNG cells into the right leg of mice (Fig. 28). Time-course images of the whole-body scan showed preferential accumulation of HSA-AD/DOX in the tumor (Fig. 29a). Similar to the results obtained from the heterotopic xenograft model, the fluorescence signal of HSA-AD/DOX at the tumor site increased continuously up to 7 h and reached a plateau (Fig. 29b). Moreover, *ex vivo* imaging revealed that the average radiant efficiency of the right legs (with tumor) was 2.83-fold higher than that of the left legs

(without tumor), supporting the bone tumor-targeting ability of HSA-AD/DOX (Fig. 30).

3.15. *In vivo* antitumor efficacy

An *in vivo* antitumor efficacy test was conducted in the hydroxyapatite-containing HOS/MNNG tumor-xenografted mice according to the therapeutic schedule presented in Fig. 31. The mice were randomly divided into four treatment groups: no intervention (untreated), free DOX (solution), HSA/DOX, and HSA-AD/DOX, and their tumor volume and body weight were monitored for 16 days. The tumor volume versus time profile revealed the highest tumor-suppressive effect of HSA-AD/DOX compared to the other formulations (Fig. 31). On day 16, the average tumor volume of the HSA-AD/DOX group was 2.68- and 1.68-fold smaller than that of the DOX solution and HSA/DOX groups, respectively, which can be explained by the improved biodistribution observed in the NIRF imaging studies. HSA/DOX also showed significantly higher antitumor efficacy than free DOX, which can be attributed to the innate tumor-targeting ability of HSA. The appearance of the dissected tumors from each group on day 16 also displayed similar tendencies (Fig. 32a). The significantly different tumor weight would confirm the enhanced *in vivo* antitumor efficacy (Fig. 32b). Although the DOX solution was moderately effective in suppressing tumor growth, it is worth noting that the average body weight in the solution

group was significantly reduced by 25.6% on day 16 compared to that in the no-intervention group, implying the development of systemic toxicity (Fig. 33). In contrast, both NC-treated groups showed a negligible body weight loss of less than 9%. These findings indicate that the developed NCs are safer and more effective than free DOX.

3.16. Histological analysis of tumors and major organs

Histological analysis was also performed on the tumors and organs excised on day 16 (Fig. 34). The degree of apoptosis of each tumor was evaluated using the terminal deoxynucleotidyl transferase dUTP nick-end labeling (TUNEL) assay. The HSA-AD/DOX group exhibited the highest degree of apoptosis compared to the other groups, which was consistent with the above-obtained results. Further, hematoxylin and eosin (H&E) staining was performed on the dissected hearts to investigate the cardiotoxicity induced by DOX [46,47], which was observed in the DOX solution group as the loss of myofibrils and striations. In contrast, the NC groups exhibited intact morphologies similar with those of the untreated group, suggesting reduced cardiotoxicity. This could be due to the improved targeting ability of albumin-based NCs compared to free DOX. No significant damage was observed in other major organs, including the liver, kidney, spleen, and lung.

3.17. Complete blood counting (CBC) analysis

For further evaluation of the DOX-and AD-related bone toxicities, the complete blood counting (CBC) was investigated after treatment. DOX solution, blank HSA-AD (*i.e.,* without drug loading), and DOX-loaded NCs were intravenously administered to Sprague-Dawley (SD) rats following the same treatment schedule as in Fig. 31. As shown in Table 6, the CBC values of the blank HSA-AD-treated group were within the reference ranges, exhibiting comparable results to those of the untreated group. These data suggest that HSA-AD has a negligible toxicity. Due to the acute toxicity myelosuppression by DOX [50], the HSA-AD/DOX-treated group showed a decreased WBC count yet within the reference range (4.5 to 11.0 × 103/μL). However, no rats were survived in the DOX solution-treated group until the last treatment (day 15), supporting that the HSA-AD-based formulation significantly reduced the acute toxicity of the anti-neoplastic drugs.

3.18. Antibody microarray analysis of NCs-treated tumors

To investigate the cell death and apoptosis of HSA-AD/DOX at a molecular level, the protein expression patterns of the dissected tumors after anticancer therapy were analyzed using antibody microarrays. Fig. 35a shows the protein expression patterns related to cell death and apoptosis as relative fold-change compared to the untreated group. All the groups markedly induced the expression changes of apoptotic- and pro-apoptotic

proteins in tumors compare to untreated group, including TP53, caspase-1, caspase-3, caspase-9, and PARP, which might support the tumor suppression observed in the tumor growth profile and histological analysis. Gene set enrichment analysis (GSEA) was conducted to analyze how these expression patterns would be related to the cell death of cancer cells (Fig. 35b). The GSEA results show that the HSA-AD/DOX treatment is positively correlated with the positive regulation of cell death and execution phase of apoptosis, which is consistent well with the doxorubicin-induced antitumor effect [48]. Fig. 35c shows the expression plots that directly compare the relative expression level of core proteins involved in the cell death. The expression of the proteins tends to increase in order of DOX solution, HSA/DOX, and HSA-AD/DOX, supporting the significance of GSEA results.

4. Conclusion

A novel alendronate-conjugated albumin-based NCs was developed for the improved distribution and tumor suppressive effects to bone tumors. The NCs were successfully fabricated *via* BMT, a newly devised method in which the native structure of albumin is preserved in contrast to conventional fabrication methods using organic solvents and crosslinkers. The enhanced tumor distribution was attributed to the conjugated AD, which was verified in newly developed tumor microenvironment-mimicking *in vitro* and *in vivo* models. The increased targeting ability of the NCs could be effectively translated into the improved therapeutic efficacy and reduced systemic toxicities, suggesting that HSA-AD/DOX is a promising delivery system for bone tumor treatment.

5. References

[1] B. Clarke, Normal bone anatomy and physiology. Clin. J. Am. Soc. Nephrol. **3**, S131-139 (2008).

https://doi.org/10.2215/CJN.04151206

[2] R. Florencio-Silva, G. R. D. S. Sasso, E. Sasso-Cerri, M. J. Simoes, P. S. Cerri, Biology of bone tissue: structure, function, and factors that influence bone cells. Biomed Res. Int. **2015**, 17−33 (2015).

https://doi.org/10.1155/2015/421746

[3] J. L. Ferguson, S. P. Turner, Bone cancer: diagnosis and treatment principles. Am Fam Physician. **98**, 205-213 (2018).

[4] H. Sugiyama, H. Kajihara, Characteristics of benign and malignant bone tumors registered in the hiroshima tumor tissue registry, 1973-2012. J. Bone Jt. Surg. **e0064** (2018).

[5] X. Zhao, Q. Wu, X. Gong, J. Liu, Y. Ma, Osteosarcoma: a review of current and future therapeutic approaches. BioMed. Eng. OnLine **20**, 1-14 (2021).

https://doi.org/10.1186/s12938-021-00860-0

[6] F. He, A.E. Chiou, H.C. Loh, M. Lynch, B.R. Seo et al., Multiscale characterization of the mineral phase at skeletal sites of breast cancer metastasis. Proc. Natl. Acad. Sci. U. S. A. **114**, 10542−10548 (2017).

https://doi.org/10.1073/pnas.1708161114

[7] J. Ritter, S.S. Bielack, Osteosarcoma. Ann. Oncol. **21**, Supplement 7, vii320−vii325 (2010).

https://doi.org/10.1093/annonc/mdq276

[8] A. Swami, M.R. Reagan, P. Basto, Y. Mishima, N. Kamaly et al., Engineered nanomedicine for myeloma and bone microenvironment targeting. Proc. Natl. Acad. Sci. U. S. A. **111**, 10287−10292 (2014).

https://doi.org/10.1073/pnas.1401337111

[9] K.R. Chaudhari, A. Kumar, V.K.M. Khandelwal, A.K. Mishra, J. Monkkonen et al., Targeting efficiency and biodistribution of zoledronate conjugated docetaxel loaded pegylated PBCA nanoparticles for bone metastasis. Adv. Funct. Mater. **22**, 4101−4114 (2012).

https://doi.org/10.1002/adfm.201102357

[10] Y. Wang, Q. Huang, X. He, H. Chen, Y. Zou et al., Multifunctional melanin-like nanoparticles for bone-targeted chemophotothermal therapy of malignant bone tumors and osteolysis. Biomaterials **183**, 10−19 (2018).

https://doi.org/10.1016/j.biomaterials.2018.08.033

[11] Z.F. Zhou, T.W. Sun, F. Chen, D.Q. Zuo, H.S. Wang et al., Calcium phosphate-phosphorylated adenosine hybrid microspheres for anti-osteosarcoma drug delivery and osteogenic differentiation. Biomaterials **121**, 1−14 (2017).

https://doi.org/10.1016/j.biomaterials.2016.12.031

[12] E. Cenni, D. Granchi, S. Avnet, C. Fotia, M. Salerno et al., Biocompatibility of poly(D,L-lactide-co-glycolide) nanoparticles conjugated with alendronate. Biomaterials **29,** 1400−1411 (2008).

https://doi.org/10.1016/j.biomaterials.2007.12.022

[13] L.E. Cole, T. Vargo-Gogola, R.K. Roeder, Targeted delivery to bone and mineral deposits using bisphosphonate ligands. Adv. Drug Delivery Rev. **99**, 12−27 (2016).

https://doi.org/10.1016/j.addr.2015.10.005

[14] Y. Matsumura, H. Maeda, A new concept for macromolecular therapeutics in cancer chemotherapy: mechanism of tumoritropic accumulation of proteins and the antitumor agent smancs. Cancer Res. **46**, 6387−6392 (1986).

[15] Blanco, E.; Shen, H.; Ferrari, M. Principles of nanoparticle design for overcoming biological barriers to drug delivery. Nat. Biotechnol. **33**, 941−951 (2015).

https://doi.org/10.1038/nbt.3330

[16] J.J. McManus, P. Charbonneau, E. Zaccarelli, N. Asherie, The physics of protein self-assembly. Curr. Opin. Colloid. Interface Sci. **22**, 73−79 (2016).

https://doi.org/10.1016/j.cocis.2016.02.011

[17] J. DeRuiter, R. Clark, Bisphosphonate: Calcium Antiresorptive Agents. Endocrine Mode, 2002

[18] S. Sindhwani, A. M. Syed, J. Ngai, B. R. kingston, L. Maiorino et. al., The entry of nanoparticles into solid tumors. Nat. Mater. **19,** 566 (2020).

https://doi.org/10.1038/s41563-019-0566-2

[19] M.R. Green, G.M. Manikhas, S. Orlov, B. Afanasyev, A.M. Makhson et al., Abraxane, a novel cremophor-free, albumin-bound particle form of paclitaxel for the treatment of advanced non-small-cell lung cancer. Ann. Oncol. **17**, 1263−1268 (2006).

https://doi.org/10.1093/annonc/mdl104

[20] W.J. Gradishar, S. Tjulandin, N. Davidson, H. Shaw, N. Desai, et al., Phase III trial of nanoparticle albumin-bound paclitaxel compared with polyethylated castor oil–based paclitaxel in women with breast cancer. J. Clin. Oncol. **23**, 7794−7803 (2005).

https://doi.org/10.1200/JCO.2005.04.937

[21] D.D.V. Hoff, T. Ervin, F.P. Arena, E.G. Chiorean, J. Infante et al, Increased survival in pancreatic cancer with nab-paclitaxel plus gemcitabine. N. Engl. J. Med. **369**, 1691−1703 (2013).

https://doi.org/10.1056/NEJMoa1304369

[22] N. Desai, V. Trieu, Z. Yao, L. Louie, S. Ci et al., Increased antitumor activity, intratumor paclitaxel concentrations, and endothelial cell transport of cremophor-free, albumin-bound paclitaxel, ABI-007, compared with cremophor-based paclitaxel. Clin. Cancer Res. **12**, 1317−1324 (2006).

https://doi.org/10.1158/1078-0432.CCR-05-1634

[23] S. Senapati, A.K. Mahanta, S. Kumar, P. Maiti, Controlled drug delivery vehicles for cancer treatment and their performance. Signal. Transduct. Target. Ther. **3**, 7 (2018).

https://doi.org/10.1038/s41392-017-0004-3

[24] S.A. Arnold, R.A. Brekken, SPARC: a matricellular regulator of tumorigenesis. J. Cell Commun. Signal. **3**, 255−273 (2009).

https://doi.org/10.1007/s12079-009-0072-4

[25] M. Tichet, V.P. Homme, N. Fenouille, D. Ambrosetti, A. Mallavialle et al., Tumour-derived SPARC drives vascular permeability and extravasation through endothelial VCAM1 signalling to promote metastasis. Nat. Commun. **6**, 6993 (2015).

https://doi.org/10.1038/ncomms7993

[26] J. Vanderburgh, J.L. Hill, M.K. Gupta, K.A. Kwakwa, S.K. Wang et al., Tuning ligand density to optimize pharmacokinetics of targeted nanoparticles for dual protection against tumor-induced bone destruction. ACS Nano **14**, 311−327 (2020).

https://doi.org/10.1021/acsnano.9b04571

[27] B. Palazzo, M. Iafisco, M. Laforgia, N. Margiotta, G. Natile et al., Biomimetic hydroxyapatite–drug nanocrystals as potential bone substitutes with antitumor drug delivery properties. Adv. Funct. Mater. **17**, 2180−2188 (2007).

https://doi.org/10.1002/adfm.200600361

[28] C. Li, Y. Zhang, G. Chen, F. Hu, K. Zhao et al, Engineered multifunctional nanomedicine for simultaneous stereotactic

chemotherapy and inhibited osteolysis in an orthotopic model of bone metastasis. Adv. Mater. **29**, 1605754 (2017).

https://doi.org/10.1002/adma.201605754

[29] W. Cui, J. Li, G. Decher, Self-assembled smart nanocarriers for targeted drug delivery. Adv. Mater. **28**, 1302−1311 (2016).

https://doi.org/10.1002/adma.201502479

[30] S. Bae, K. Ma, T.H. Kim, E.S. Lee, K.T. Oh et al., Doxorubicin-loaded human serum albumin nanoparticles surface-modified with TNF-related apoptosis-inducing ligand and transferrin for targeting multiple tumor types. Biomaterials **33**, 1536−1546 (2012).

https://doi.org/10.1016/j.biomaterials.2011.10.050

[31] F.F. An, X.H. Zhang, Strategies for preparing albumin-based nanoparticles for multifunctional bioimaging and drug delivery. Theranostics **7**, 3667−3689 (2017).

https://doi.org/10.7150/thno.19365

[32] D. Braga, F. Grepioni, Reactions between or within molecular crystals. Angew. Chem. Int. Ed. Engl. **43**, 4002−4011 (2004).

https://doi.org/10.1002/anie.200301721

[33] J.L. Howard, Y. Sagatov, L. Repusseau, C. Schotten, D.L. Browne, Controlling reactivity through liquid assisted grinding: the curious case of mechanochemical fluorination. Green Chem. **19**, 2798−2802 (2017).

https://doi.org/10.1039/C6GC03139K

[34] S.L. James, C.J. Adams, C. Bolm, D. Braga, P. Collier et al., Mechanochemistry: opportunities for new and cleaner synthesis. Chem. Soc. Rev. **41**, 413−447 (2012).

https://doi.org/10.1039/C1CS15171A

[35] N.K. Ibrahim, N. Desai, S. Legha, P. Soon-Shiong, R.L. Theriault et al., Phase I and pharmacokinetic study of ABI-007, a cremophor-free, protein-stabilized, nanoparticle formulation of paclitaxel. Clin. Cancer Res. **8**, 1038−1044 (2002).

[36] J.E. Schiel, C.M. Ohnmacht, D.S. Hage, Measurement of drug-protein dissociation rates by high-performance affinity chromatography and peak profiling. Anal. Chem. **81**, 4320−4333 (2009).

https://doi.org/10.1021/ac9000404

[37] J.Y. Lee, S.J. Chung, H.J. Cho, D.D. Kim, Phenylboronic acid-decorated chondroitin sulfate A-based theranostic nanoparticles for enhanced tumor targeting and penetration. Adv. Funct. Mater. **25**, 3705−3717 (2015).

https://doi.org/10.1002/adfm.201500680

[38] L. Palanikumar, S. Al-Hosani, M. Kalmouni, V.P. Nguyen, L. Ali et al., pH-responsive high stability polymeric nanoparticles for targeted delivery of anticancer therapeutics. Commun. Biol. **3**, 95 (2020).

https://doi.org/10.1038/s42003-020-0817-4

[39] S.U. Lauvrak, E. Munthe, S.H. Kresse, E.W. Stratford, H.M. Namløs et al., Functional characterisation of osteosarcoma cell lines and identification of mRNAs and miRNAs associated with aggressive cancer phenotypes. Br. J. Cancer **109**, 2228−2236 (2013).

https://doi.org/10.1038/bjc.2013.549

[40] S.M. Davidson, O. Jonas, M.A. Keibler, H.W. Hou, A. Luengo et al., Direct evidence for cancer-cell-autonomous extracellular protein catabolism in pancreatic tumors. Nat. Med. **23**, 235−241 (2016).

https://doi.org/10.1038/nm.4256

[41] C. Commisso, S.M. Davidson, R.G. Soydaner-Azeloglu, S.J. Parker, J.J. Kamphorst et al., Macropinocytosis of protein is an amino acid supply route in ras-transformed cells. Nature **497**, 633−637 (2013).

https://doi.org/10.1038/nature12138

[42] M. Chatterjee, E. Ben-Josef, R. Robb, M. Vedaie, S. Seum et al., Caveolae-mediated endocytosis is critical for albumin cellular uptake and response to albumin-bound chemotherapy. Cancer Res. **77**, 5925−5937 (2017).

https://doi.org/10.1158/0008-5472.CAN-17-0604

[43] M. Pazianas, Osteonecrosis of the jaw and the role of macrophages. J. Natl. Cancer Inst. **103**, 232−240 (2011).

https://doi.org/10.1093/jnci/djq516

[44] H. Hyun, J. Park, K. Willis, J.E. Park, L.T. Lyle et al., Surface modification of polymer nanoparticles with native albumin for enhancing drug delivery to solid tumors. Biomaterials **180**, 206−224 (2018).

https://doi.org/10.1016/j.biomaterials.2018.07.024

[45] X. Zhu, R. Tang, S. Wang, X. Chen, J. Hu, C. Lei, Y. Huang, H. Wang, Z. Nie, S. Yao, Protein@inorganic nanodumpling system for high-loading protein delivery with activatable fluorescence and magnetic resonance bimodal imaging capabilities, ACS Nano 14 (2020) 2172–2182.

https://doi.org/10.1021/acsnano.9b09024

[46] A. Roessner, Biological Characterization of Bone Tumors, First ed., Springer, Berlin, 1989

[47] H. Paul, A.J. Reginato, H.R. Schumacher, Alizarin red S staining as a screening test to detect calcium compounds in synovial fluid. Arthritis Rheumatol. **26**, 191−200 (1983).

https://doi.org/10.1002/art.1780260211

[48] Y. Ichikawa, M. Ghanefar, M. Bayeva, R. Wu, A. Khechaduri et al., Cardiotoxicity of doxorubicin is mediated through mitochondrial iron accumulation. J. Clin. Invest. **124**, 617−630 (2014).

https://doi.org/10.1172/JCI72931

[49] S. Zhang, X. Liu, T. Bawa-Khalfe, L.S. Lu, Y.L. Lyu et al., Identification of the molecular basis of doxorubicin-induced cardiotoxicity. Nat. Med. **18**, 1639−1642 (2012).

https://doi.org/10.1038/nm.2919

[50] E. Blanco, H. Shen, M. Ferrari, Principles of nanoparticle design for overcoming biological barriers to drug delivery, Nat. Biotechnol. 33 (2015) 941-951.

https://doi.org/10.1038/nbt.3330

6. Tables

Table 1. Optimized process parameters of BMT for the fabrication of DOX-loaded NCs

HSA or HSA-AD (mg)	DOX (mg)	Solvent[a] (µL)	Milling rpm	Milling time (min)
20	40	50	50	3

[a] Solvent = 9.5 % DMSO in PBS

Table 2. Physicochemical properties of the NCs

Nanoclusters (NCs)	Mean diameter (nm)	Polydispersity index	Zeta-potential (mV)	Drug content (%)
HSA/DOX	163 ± 3	0.165 ± 0.010	-21.1 ± 1.5	6.13 ± 0.20
HSA-AD/DOX	161 ± 4	0.146 ± 0.030	-42.1 ± 9.6	6.11 ± 0.29

Table 3. DOX content of HSA/DOX and HSA-AD/DOX prepared by vortex-mixing or BMT

Loading method	Preparation time	DOX content (%)
HSA/DOX by vortex-mixing	12 h	0.397 ± 0.003
HSA-AD/DOX by vortex-mixing	12 h	0.309 ± 0.003
HSA/DOX by BMT	3 min	6.13 ± 0.20
HSA-AD/DOX by BMT	3 min	6.11 ± 0.29

Table 4. Content of secondary structure motif, as calculated from CD spectral analysis.

Groups	α-helix (%)	β-turn (%)	Parallel (%)	Antiparallel (%)	Random coil (%)
HSA	67.1 ± 0.3	12.2 ± 0.1	3.1 ± 0.2	3.2 ± 0.1	15.2 ± 0.1
Heat-denatured HSA	19.8 ± 0.1	18.7 ± 0.1	14.8 ± 0.2	11.5 ± 0.2	47.0 ± 0.1
HSA NPs[a]	9.9 ± 0.1	22.4 ± 0.1	23.5 ± 1.7	18.6 ± 0.1	60.9 ± 0.2
HSA-AD NPs[a]	22.8 ± 0.3	18.3 ± 0.1	13.0 ± 0.2	10.6 ± 0.1	43.0 ± 0.3
HSA-AD	59.4 ± 0.3	13.1 ± 0.1	4.2 ± 0.1	4.1 ± 0.1	19.0 ± 0.1
HSA/DOX NCs	57.7 ± 1.1	13.4 ± 0.2	4.3 ± 0.2	4.1 ± 0.1	19.4 ± 0.5
HSA-AD/DOX NCs	56.7 ± 2.7	13.5 ± 0.3	4.5 ± 0.4	4.4 ± 0.3	20.2 ± 1.3

[a]Conventional albumin NPs prepared using the solvent displacement method described in the experimental section.

Table 5. Kinetic modelling of DOX release from HSA-AD/DOX at various pH values.

Groups	pH	First-order with F_{max}			Higuchi		Baker-Lonsdale		Korsmeyer-Peppas			Peppas-Sahlin			
		R^2	k	F_{max}	R^2	k_H	R^2	k_{BL}	R^2	k_{KP}	n	R^2	k_1	k_2	m
HSA /DOX	7.4	0.983	0.050	41.7	0.927	4.77	0.931	0.0005	0.927	4.78	0.500	0.975	2.75	-0.045	0.792
HSA-AD /DOX	7.4	0.990	0.116	36.5	0.737	4.76	0.783	0.0005	0.855	9.30	0.330	0.968	6.55	-0.271	0.619
	6.8	0.981	0.124	47.8	0.784	6.36	0.850	0.001	0.929	12.6	0.325	0.977	10.6	-0.553	0.522
	5.5	0.989	0.084	65.2	0.873	8.15	0.915	0.002	0.905	12.1	0.400	0.969	8.38	-0.260	0.662

F_{max} is the maximum cumulative release, and k, k_H, k_{BL}, k_{KP}, k_1, and k_2 are the release rate constants of the corresponding models.

Table 6. Complete blood count (CBC) analysis in rats after treatment.

	RBC (x 10^6/μL)	WBC (x 10^3/μL)	Platelet (x 10^3/μL)	Hct (%)
Untreated	6.97 ± 0.73	6.94 ± 2.97	913 ± 79	44.8 ± 3.7
Blank HSA-AD	6.58 ± 0.33	7.12 ± 3.82	1192 ± 207	43.3 ± 1.6
HSA/DOX	6.82 ± 0.42	4.21 ± 1.83	1004 ± 98	44.7 ± 2.3
HSA-AD/DOX	6.73 ± 0.63	5.46 ± 2.36	1164 ± 243	41.5 ± 3.4

7. Figures

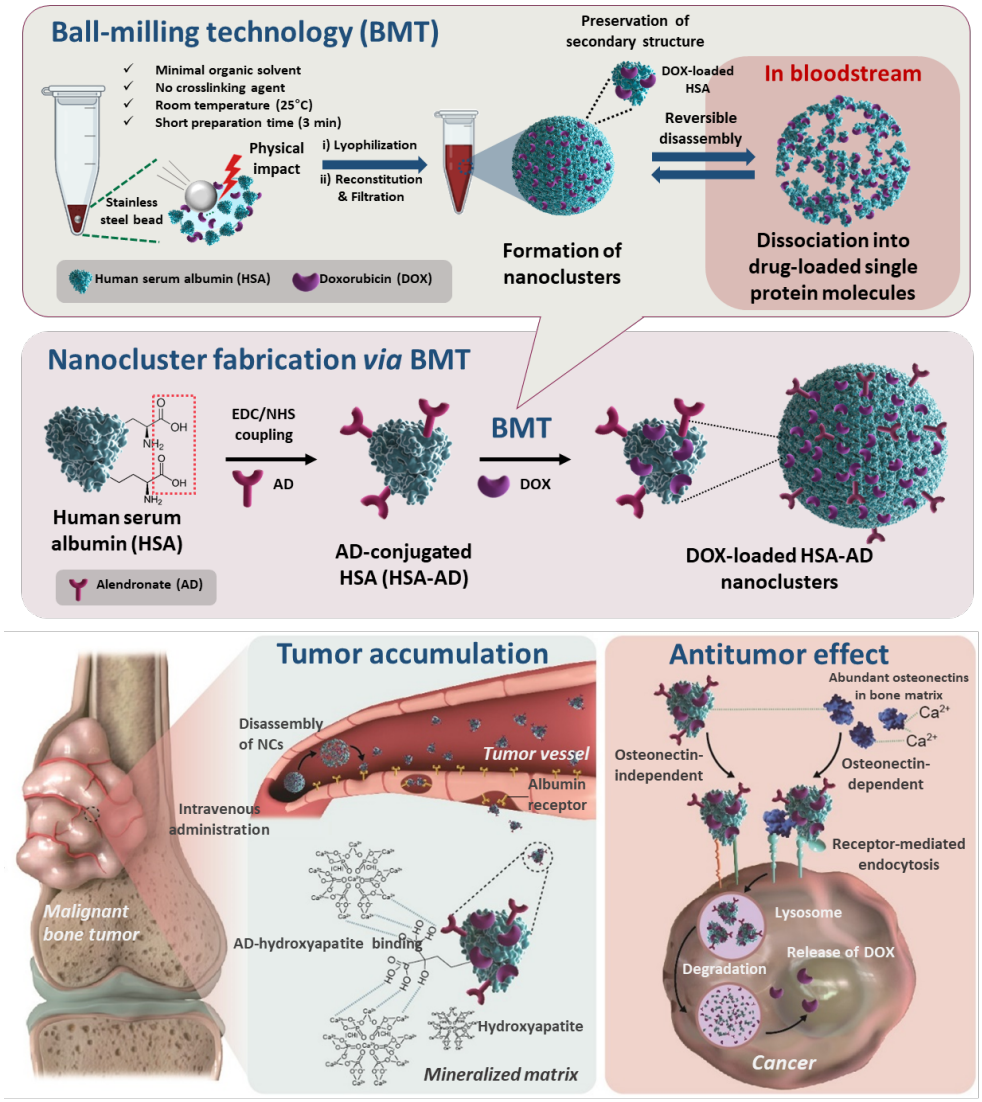

Figure 1. Schematic illustration showing the fabrication of nanoclusters *via* BMT and its mechanism of targeting the bone tumor microenvironment

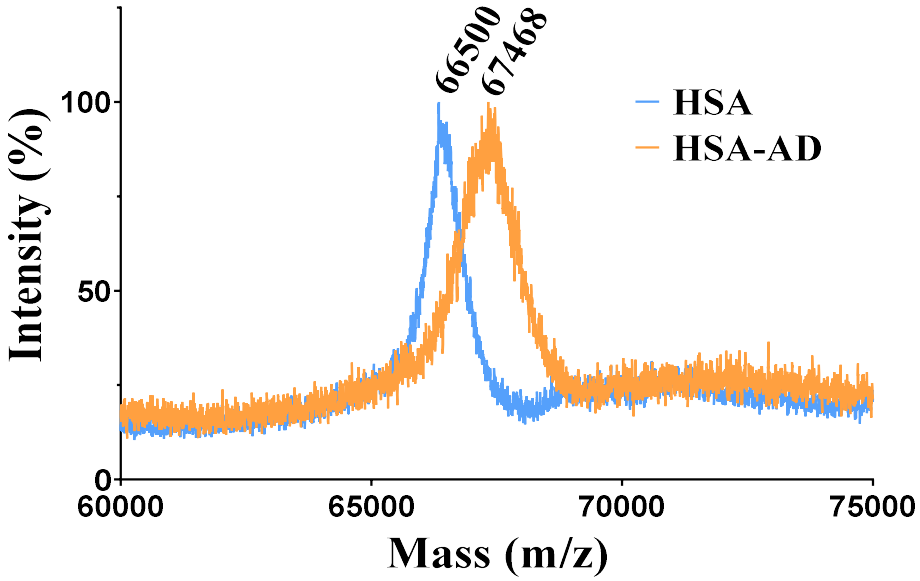

Figure 2. Analysis of molecular weight change after synthesis by Maldi-TOF.

(A)

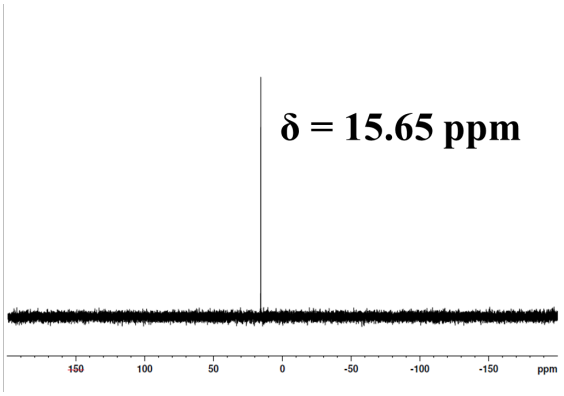

(B)

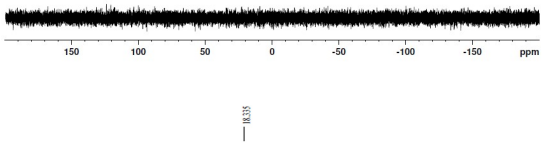

(C)

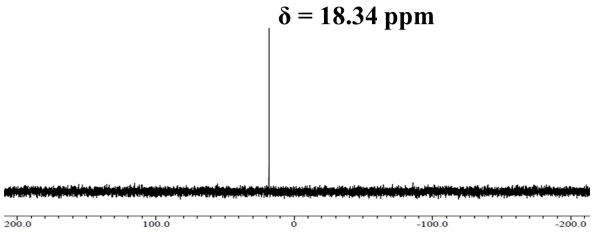

Figure 3. ^{31}P-NMR analysis of (a) HSA-AD, (b) HSA, and (c) free AD

(A)

	Mean diameter (nm)	PDI
HSA NPs	279.4 ± 3.4	0.129 ± 0.002
HSA-AD NPs	277.1 ± 5.5	0.156 ± 0.003

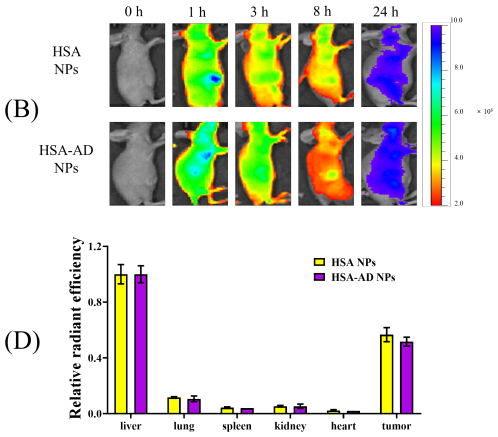

Figure 4. *In vivo* NIRF images of Cy5.5-labeled HSA or HSA-AD NPs made by desolvation method. (a) Mean diameter of the Cy5.5-conjugated NPs. (b) Representative time-dependent fluorescence images of the Cy5.5-conjugated HSA or HSA-AD NPs. (c) The *ex vivo* fluorescence image of the tumor and major organs at 24 h after IV injection, and (d) their relative radiant efficiency values. Each value was normalized by average liver radiant efficiency.

Figure 5. Digital image of DOX and the NCs in DDW. All groups were prepared as a DOX concentration of 1 mg/mL.

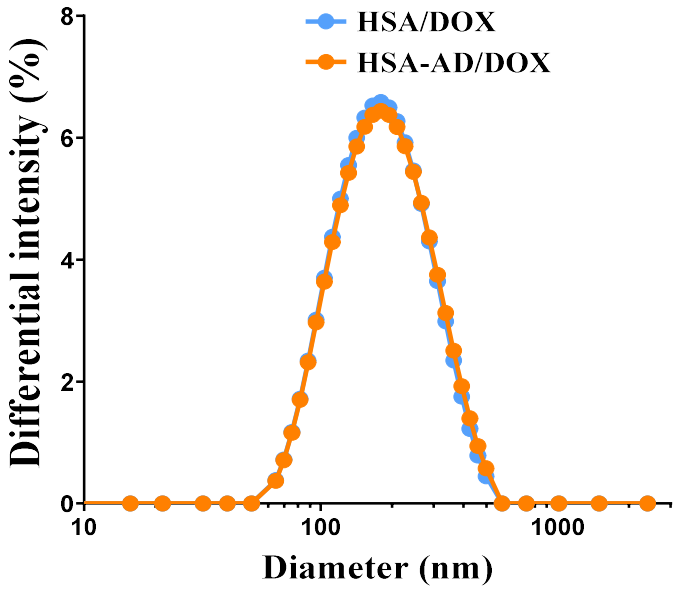

Figure 6. The size distribution of NCs, plotted against the differential intensity.

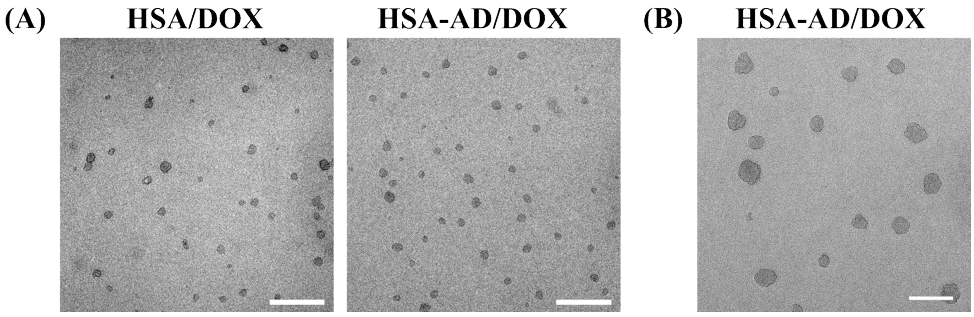

Figure 7. TEM images of HSA/DOX and HSA-AD/DOX. The length of the scale bar in (a) and (b) is 500 nm and 200 nm, respectively.

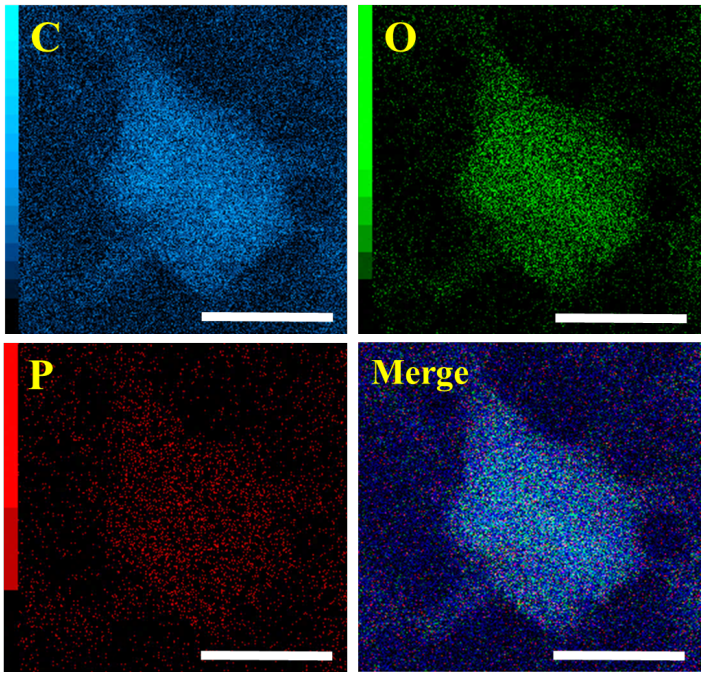

Figure 8. Atomic analysis of HSA-AD/DOX. C, O, and P indicate carbon, oxygen, and phosphorus, respectively. The length of the scale bar is 100 nm.

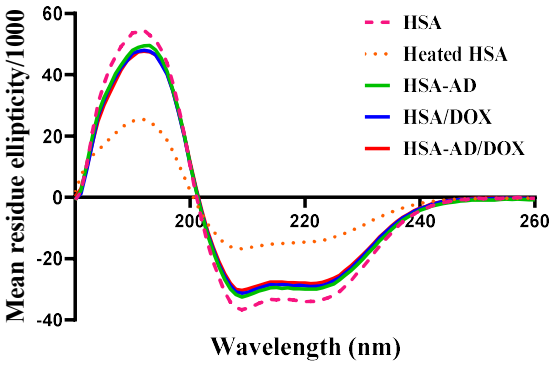

Figure 9. Circular dichroism spectra. The heat-denatured sample (orange dotted line) was heated at 80 ℃ for 30 min. All the samples were prepared at a concentration of 0.1 mg/mL.

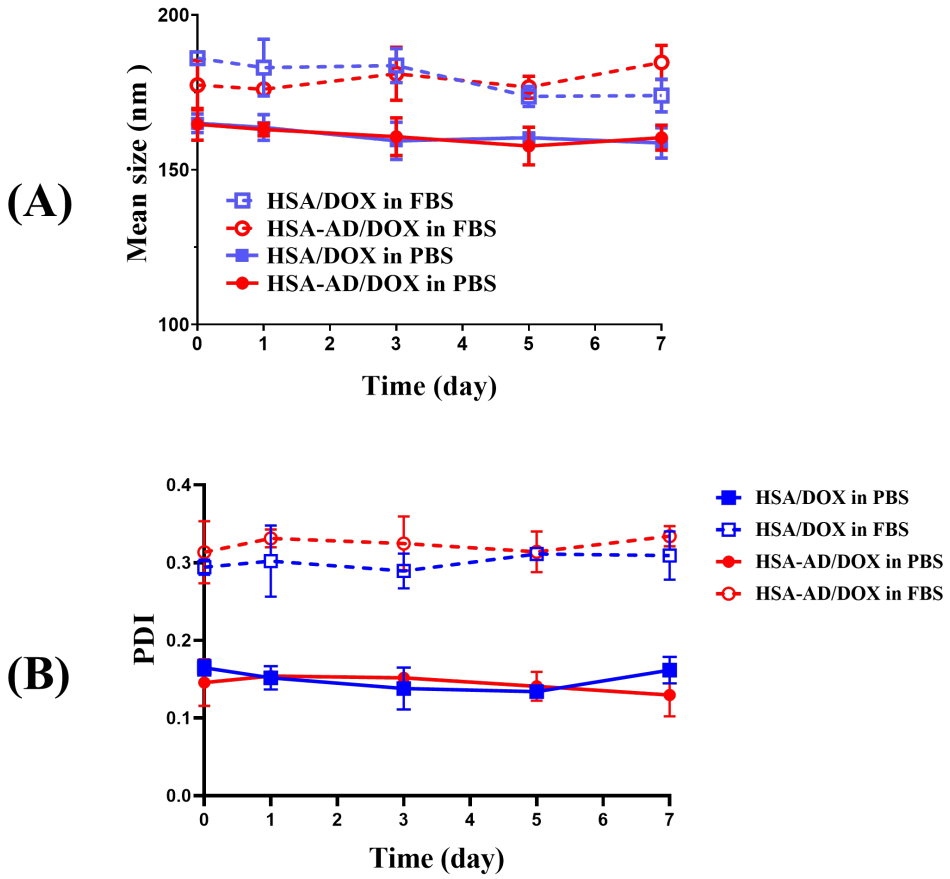

Figure 10. Mean diameter analyzes of NCs in PBS (solid line) or FBS (dotted line) for 7 days. (a) Mean diameter. (b) Polydispersity index (PDI) values of each day.

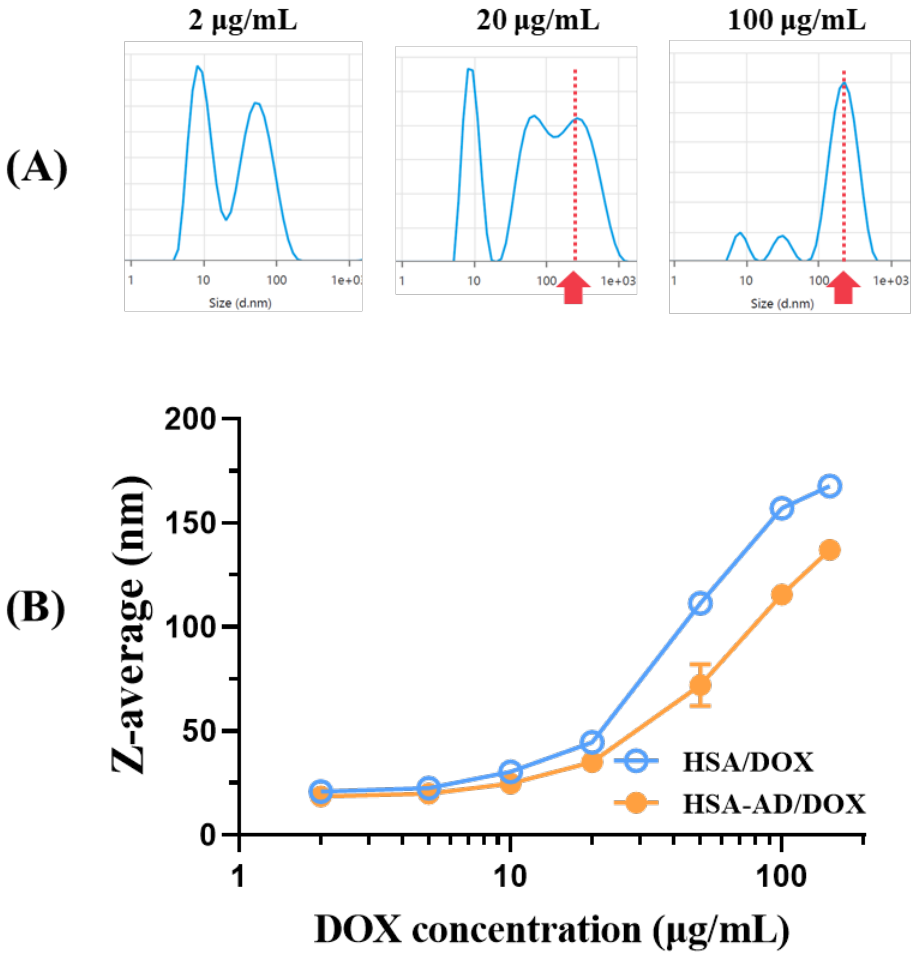

Figure 11. Disassembly of the developed NCs upon dilution. (a) Representative size distribution plot of the DOX-loaded NCs according to the differential intensity at three different concentrations. The red arrow indicates the modal value of the NCs peak with an average size of approximately 150–200 nm. (b) The mean diameter changes of HSA/DOX and HSA-AD/DOX according to the different DOX concentrations.

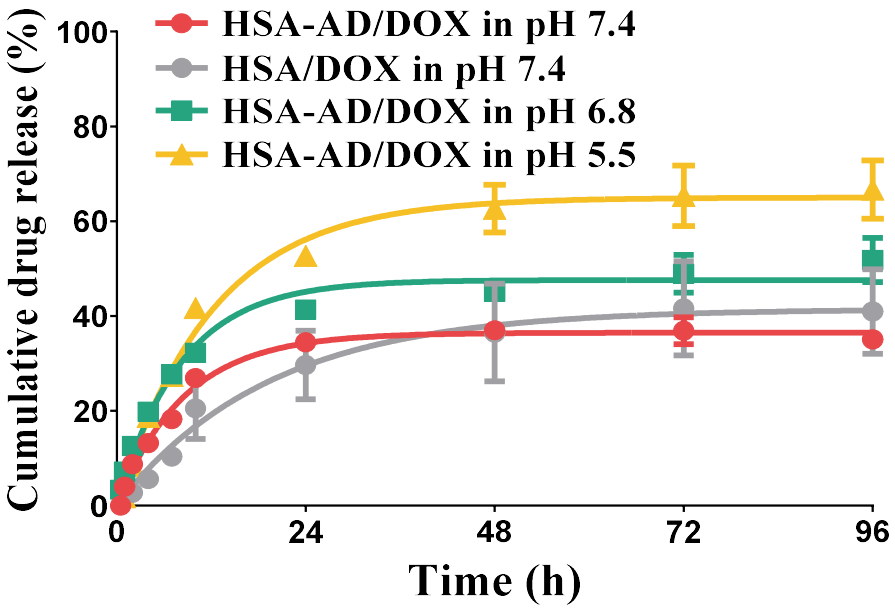

Figure 12. The cumulative drug release profile of the NCs in PBS with three different pH for 96 h.

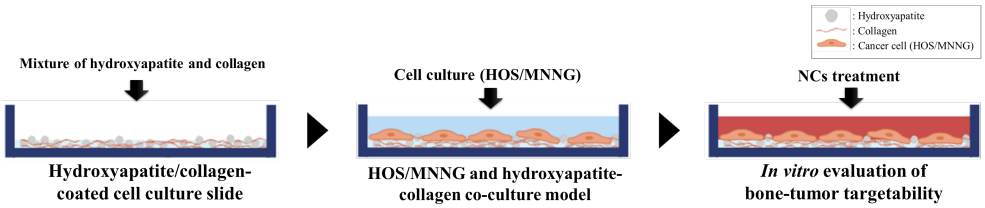

Figure 13. Scheme of HOS/MNNG cells and hydroxyapatite beads/collagen co-culture model that is designed to simulate the bone tumor microenvironment

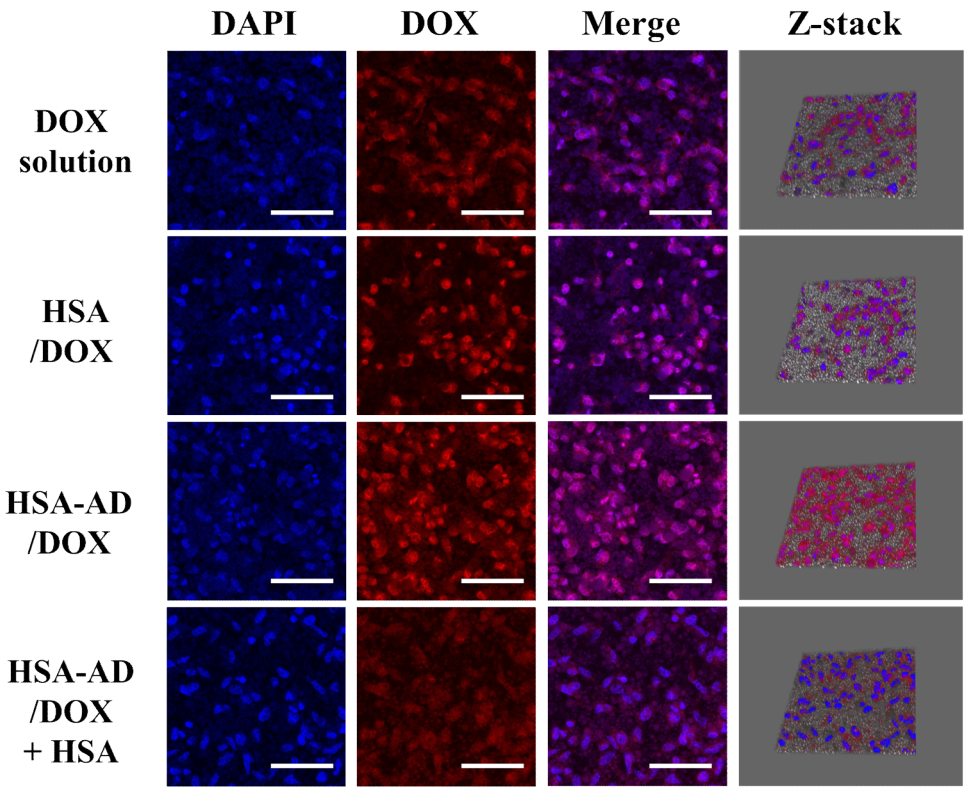

Figure 14. CLSM images in 2D cell culture model after incubation of DOX solution, HSA/DOX, HSA-AD/DOX, and HSA-AD/DOX + HSA. The length of the scale bar is 100 μm.

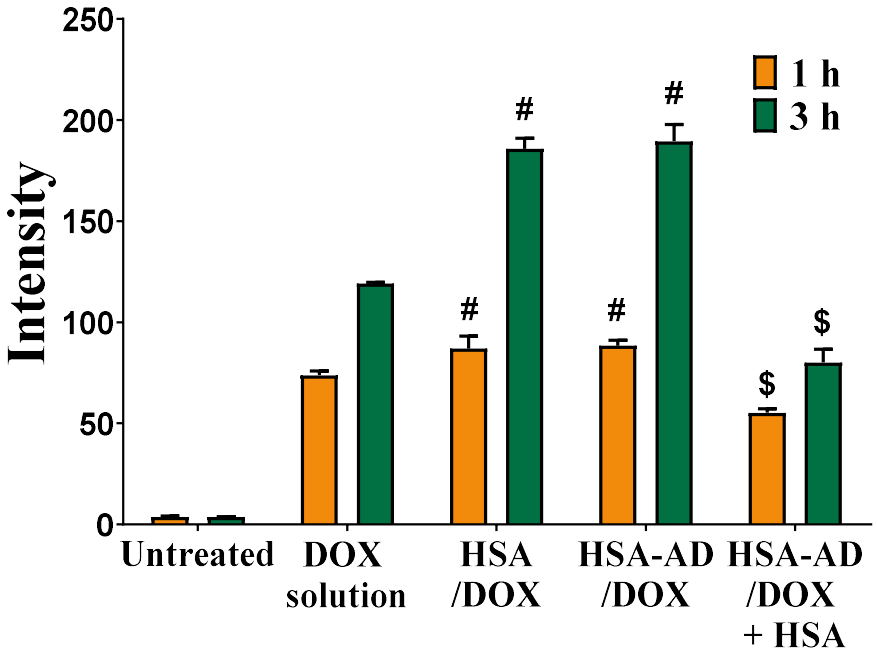

Figure 15. Flow cytometry analysis of HOS/MNNG cells after incubation for 1 and 3 h. Free HSA was used as a competitive inhibitor of receptor-mediated endocytosis of HSA-AD/DOX. $^{\#}p < 0.0001$, compared to DOX solution; $^{\$}p < 0.0001$, compared to HSA-AD/DOX.

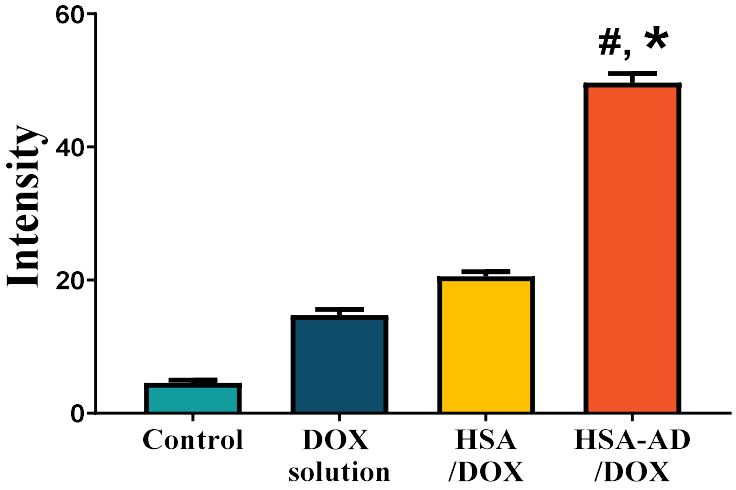

Figure 16. Flow cytometry analysis of hydroxyapatite beads after incubation with the DOX solution or NCs. $^{\#}p < 0.0001$, compared to DOX solution; $^{*}p < 0.0001$, compared to HSA/DOX.

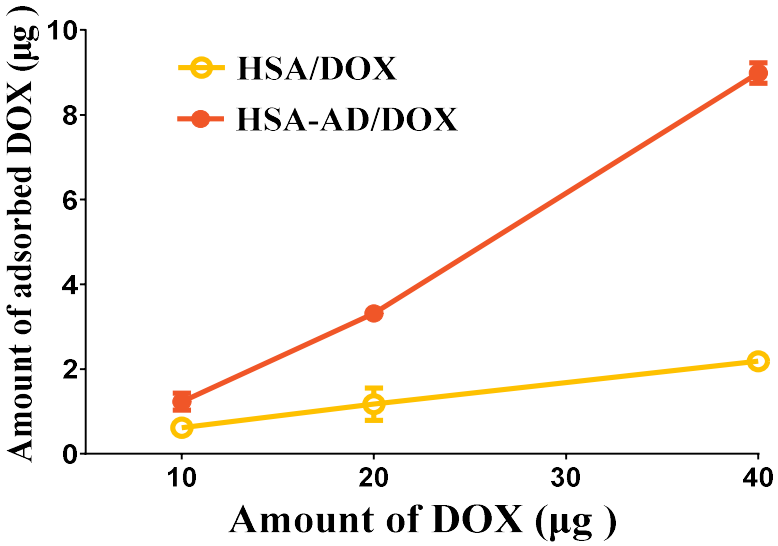

Figure 17. Measurement of the amount of adsorbed NCs to hydroxyapatite beads using UV-vis spectrophotometry. The three different amounts of NCs (10, 20, and 30 μg as DOX amount) were added to hydroxyapatite beads (10 mg).

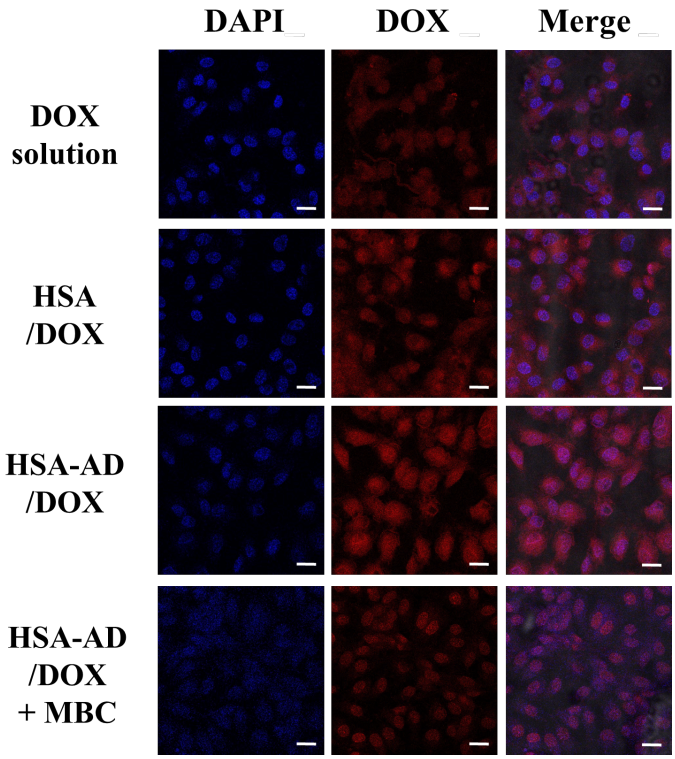

Figure 18. CLSM images of HUVECs after incubation of DOX solution, HSA/DOX, HSA-AD/DOX, and HSA-AD + MBC. The methyl-β-cyclodextrin (MBC) was used as a caveolae-mediated endocytosis inhibitor. The length of the scale bar is 20 μm.

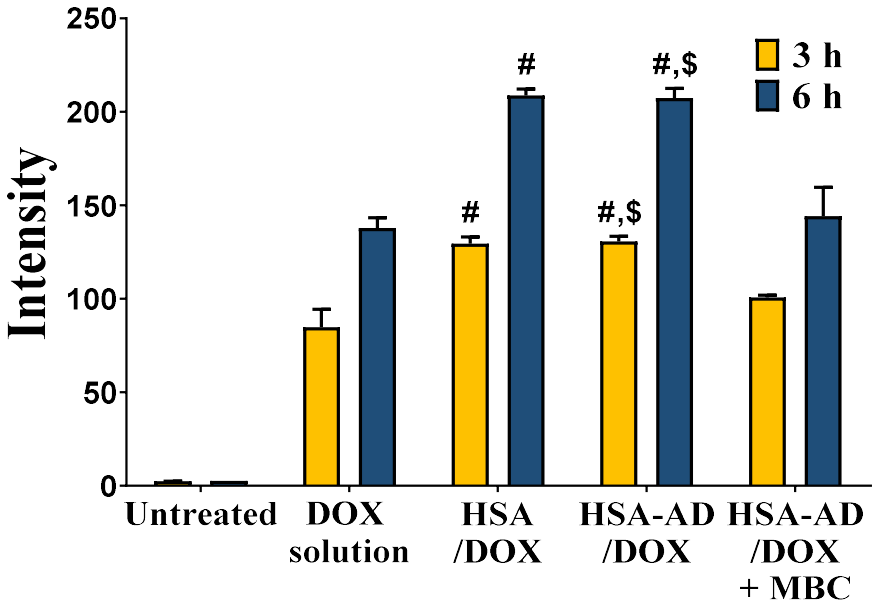

Figure 19. Flow cytometry analysis of HUVECs after incubation. The untreated group was the cells without treatment. $^{\#}p < 0.0001$, compared to DOX solution; $^{\$}p < 0.0001$, compared to HSA-AD/DOX + MBC.

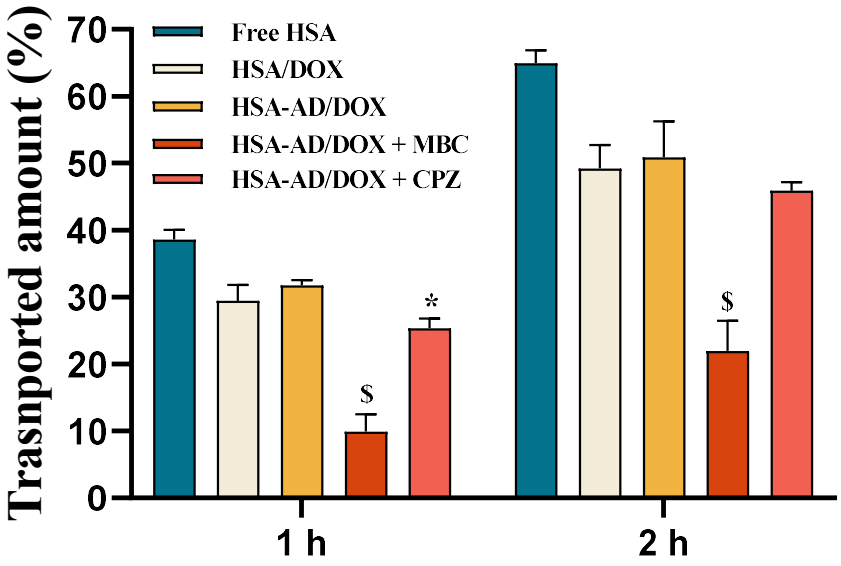

Figure 20. Transwell study in HUVECs after incubation for 1 and 2 h. The free HSA and CPZ were used as a positive control and clathrin-mediated endocytosis inhibitor, respectively. $^{*}p < 0.05$ and $^{\$}p < 0.0001$, compared to HSA-AD/DOX.

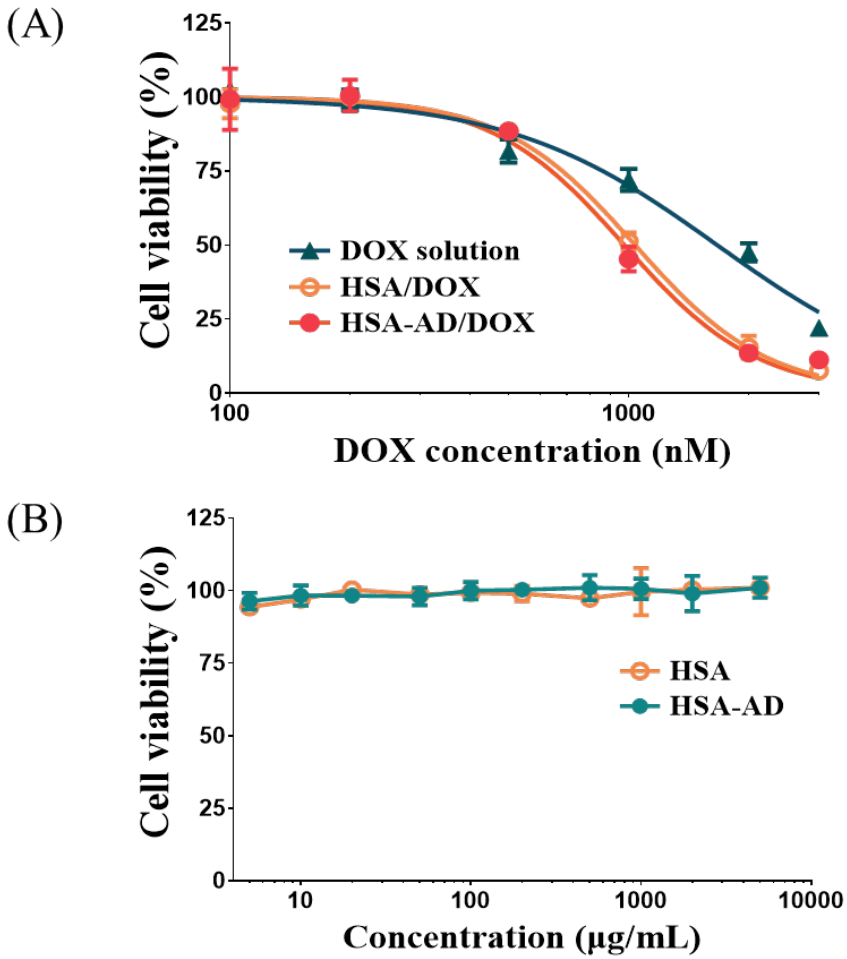

Figure 21. Cytotoxicity studies of (a) the DOX solution and NCs, and (b) blank HSA and HSA-AD (*i.e.,* DOX-unleaded HSA and HSA-AD) in HOS/MNNG cells.

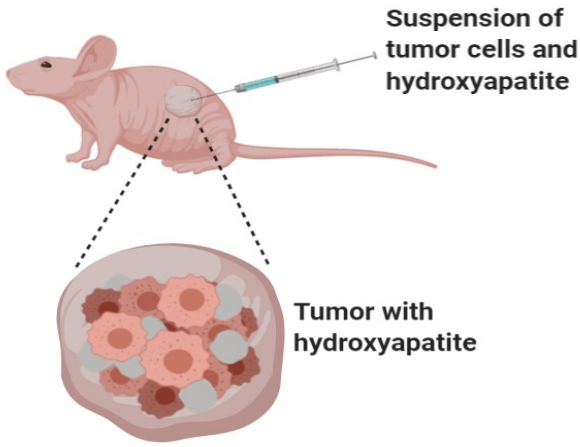

Figure 22. Scheme of hydroxyapatite-co-inoculated HOS/MNNG xenografted mouse model.

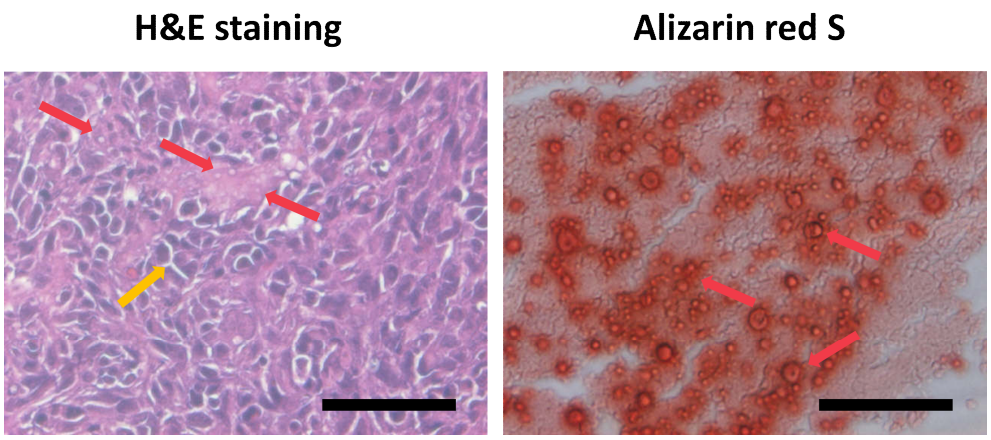

Figure 23. Histological images of the hydroxyapatite-containing xenografted tumor. Yellow and red arrows indicate the cancer cells and hydroxyapatites, respectively. The length of the scale bar is 100 μm.

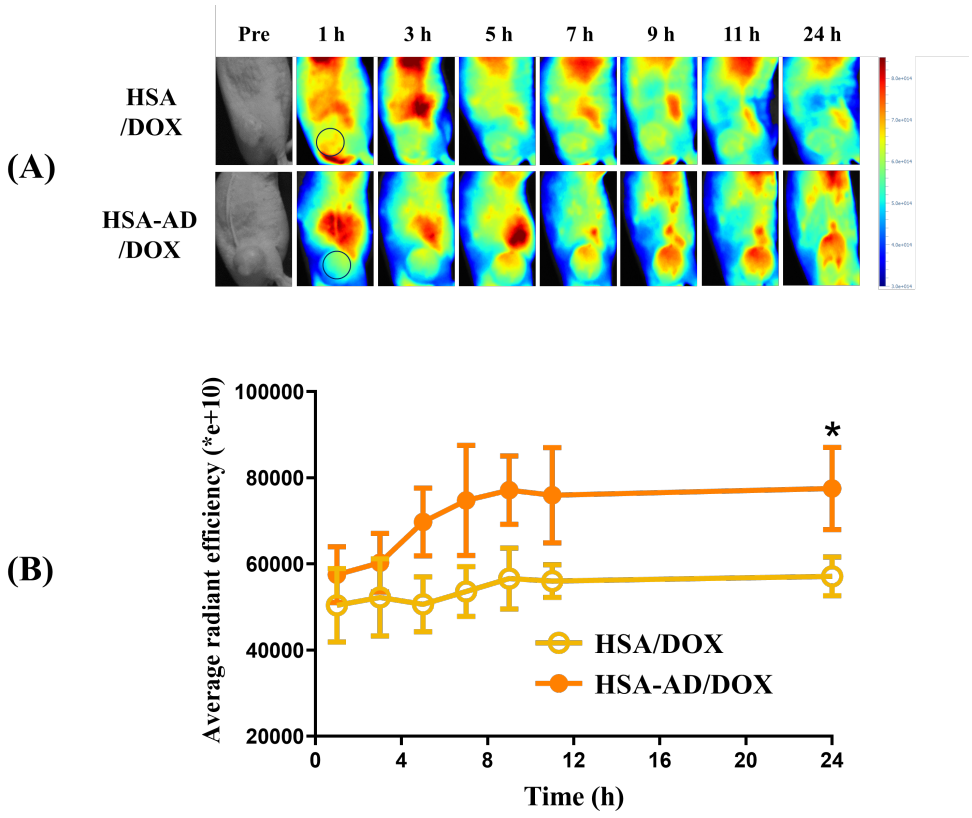

Figure 24. NIRF images of hydroxyapatite-containing HOS/MNNG xenografted mouse. (a) Whole-body scan after intravenous injection of Cy5.5-labeled HSA/DOX or HSA-AD/DOX. The circle indicates the xenografted tumor (b) Average radiant efficiency of HSA/DOX and HSA-AD/DOX, plotted against time. $^{*}p < 0.05$.

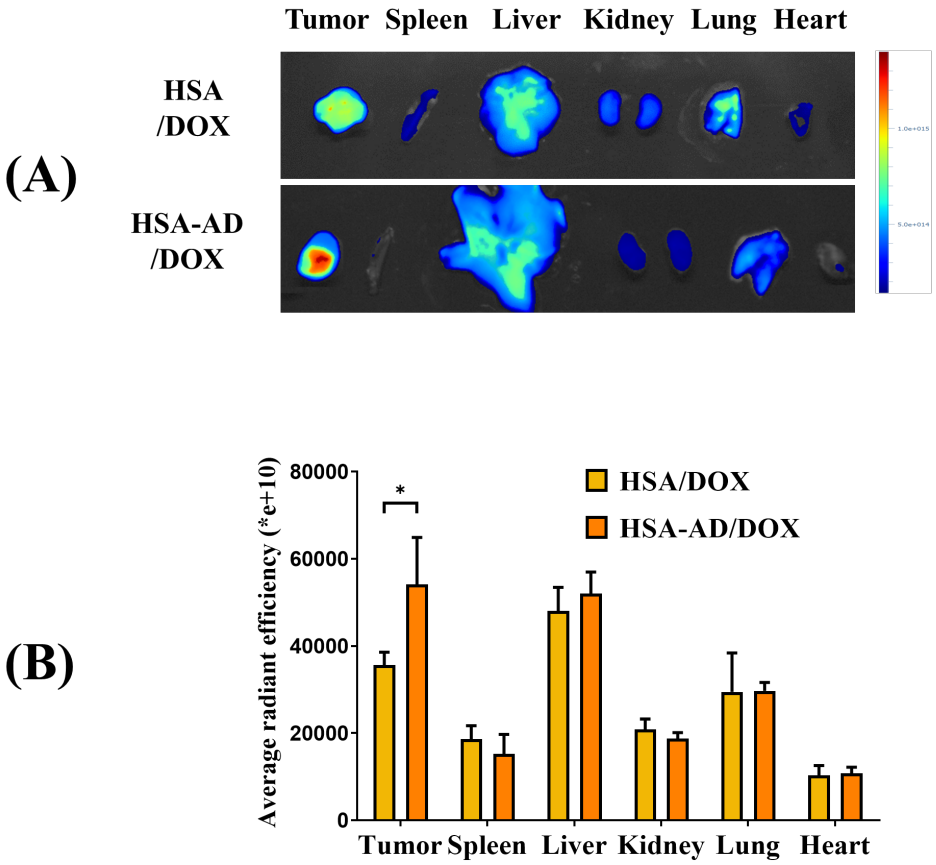

Figure 25. *Ex vivo* analysis of tumors and major organs 24 h after intravenous administration of Cy5.5-labeled NCs. (a) NIRF images of the representative mouse from each group, and (b) its average radiant efficiency values. *$p < 0.05$.

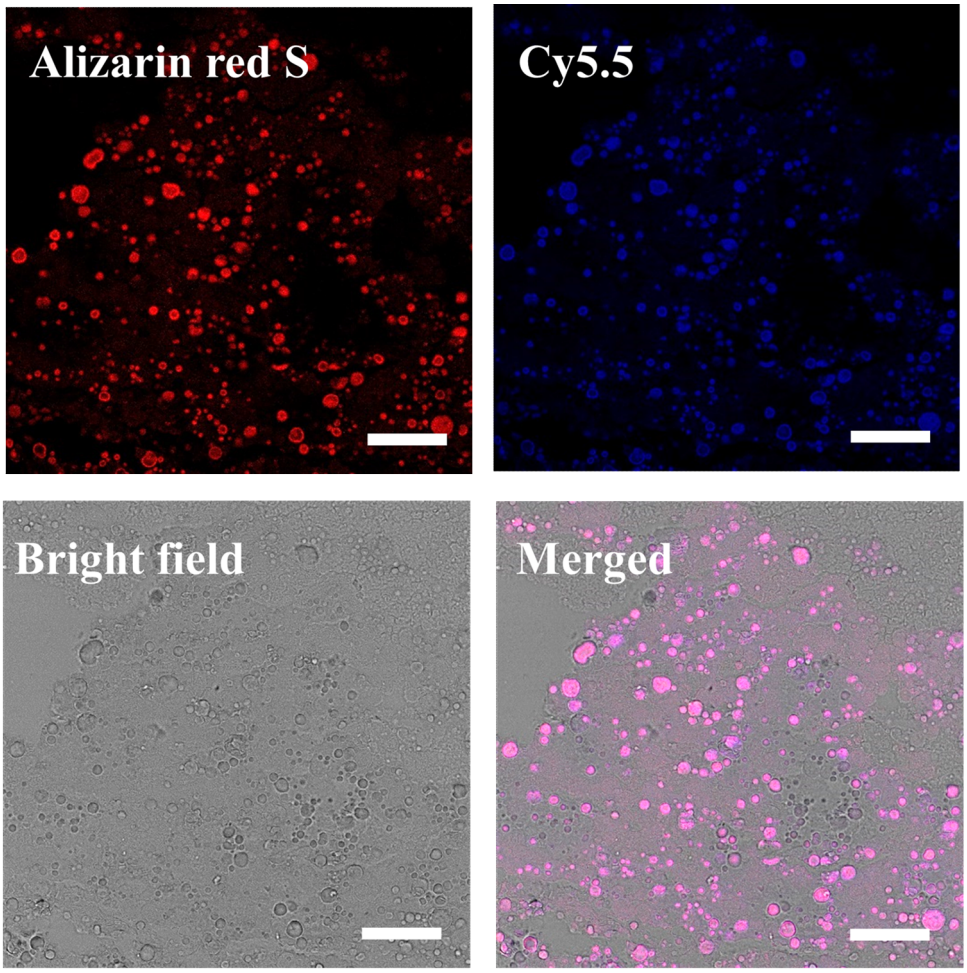

Figure 26. Histological analysis of the dissected tumor after intravenous administration of Cy5.5-labeled HSA-AD/DOX. Red and blue colors indicate the alizarin red S and Cy5.5, respectively. The fluorescence was observed by CLSM. The length of the scale bar is 50 μm.

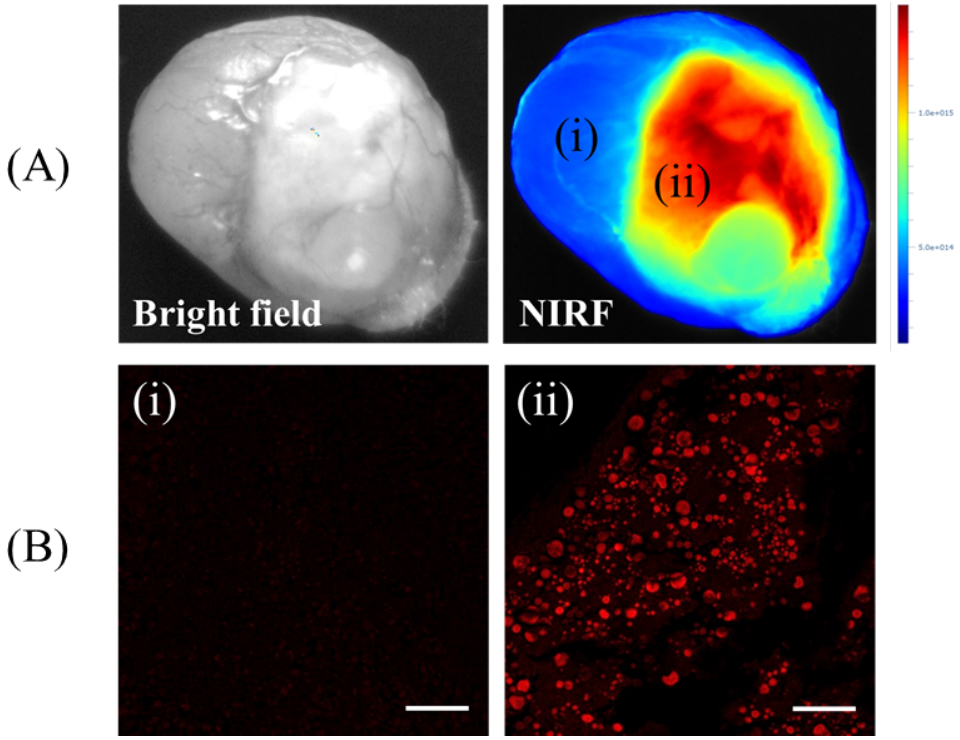

Figure 27. Preferential distribution of Cy5.5-labeled HSA-AD/DOX to the tumor region containing hydroxyapatites. (a) *Ex vivo* NIRF image of the whole tumor at 24 h post-injection. (b) Histological analyses of tumor region (i) and (ii). The red color indicates the hydroxyapatites stained with alizarin red S. The length of the scale bar is 50 μm.

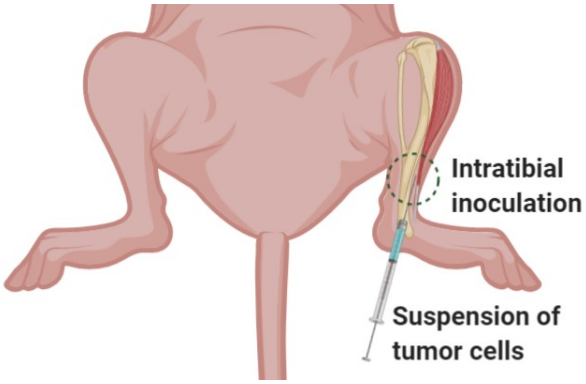

Figure 28. Scheme of orthotopic bone tumor mouse modeling. The HOS/MNNG cells were intratibially inoculated into the left leg of the mouse.

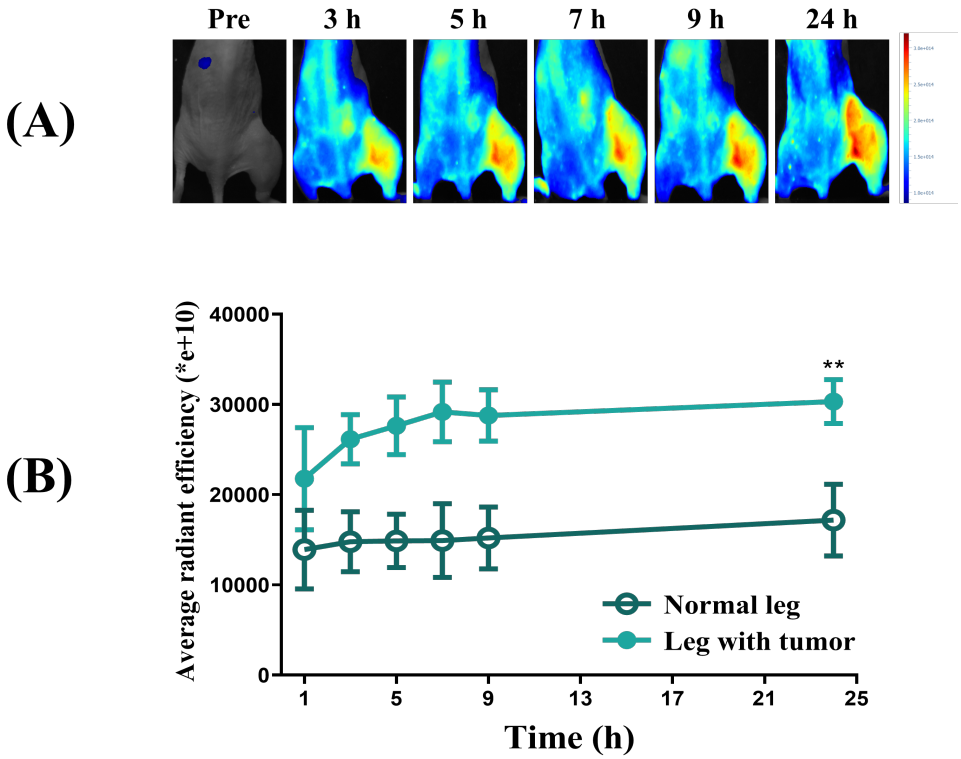

Figure 29. NIRF image of mice with intratibially inoculated tumor. (a) Time-course fluorescence images of Cy5.5-labeled HSA-AD/DOX. (b) The average radiant efficiency of legs with or without tumor.

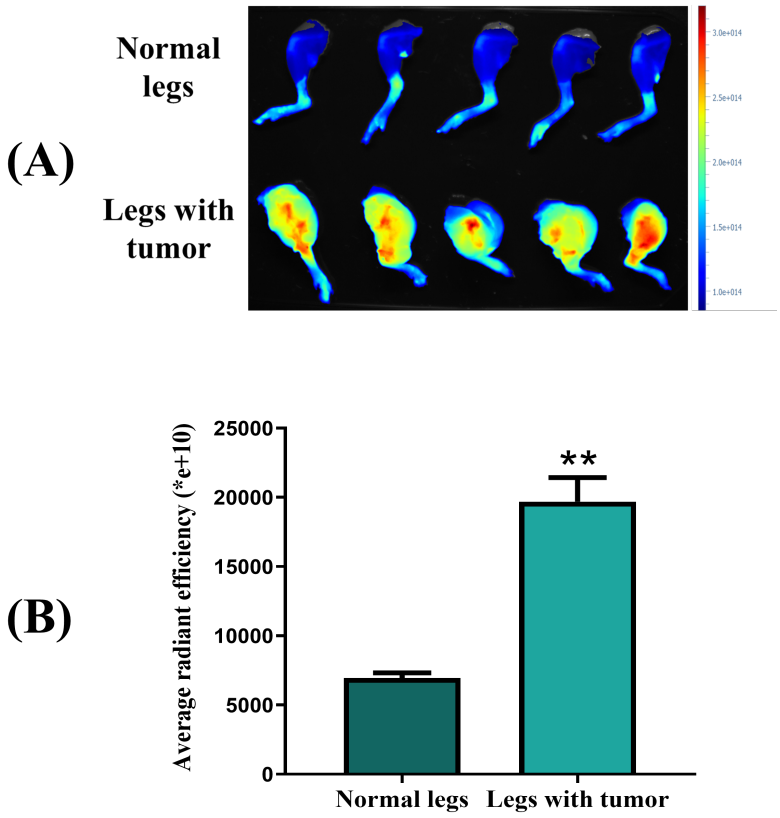

Figure 30. *Ex vivo* analysis of tumor-bearing legs. (a) Fluorescence image of the normal (legs without tumor) and tumor-bearing legs. (b) Average radiant efficiency of the dissected legs.

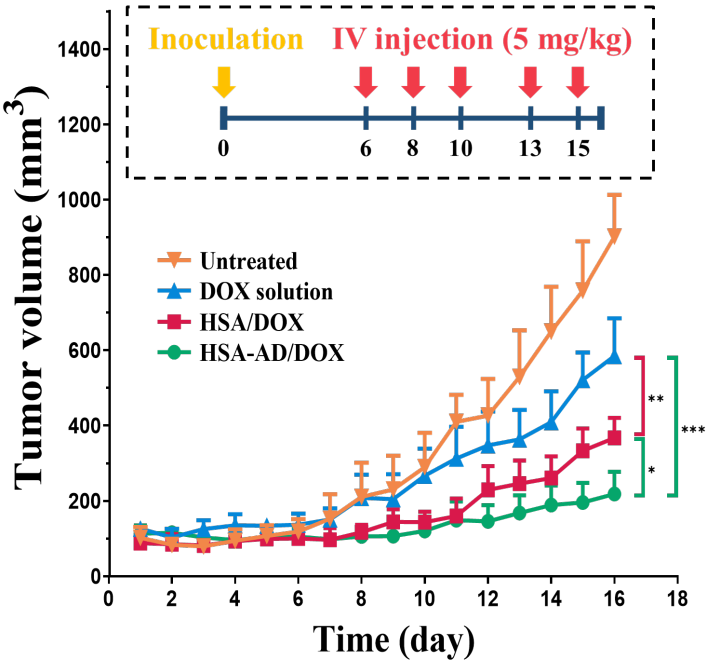

Figure 31. Tumor growth profile of the hydroxyapatite-containing HOS/MNNG-xenografted mice. The mice were treated with DOX solution, HSA/DOX, and HSA-AD/DOX five times as scheduled (dotted square).

(A)

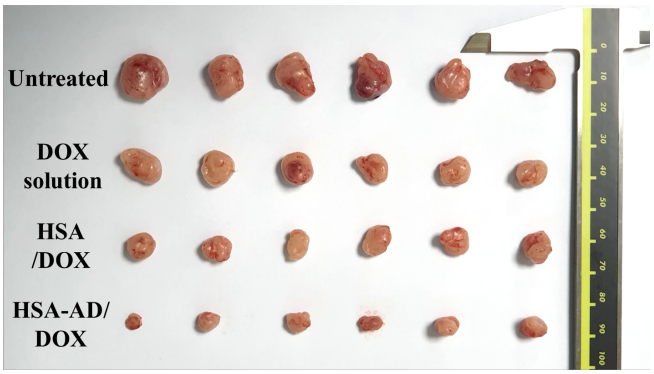

(B)

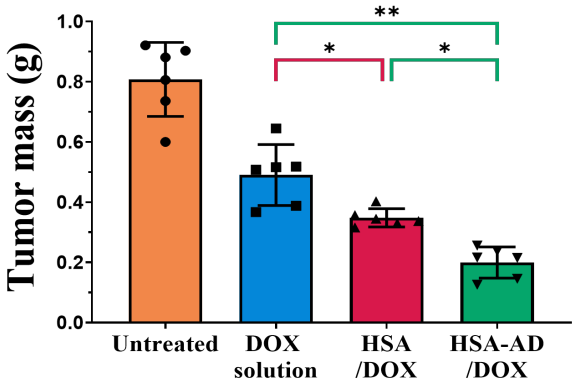

Figure 32. *Ex vivo* analysis of tumors on day 16. (a) Digital image of the excised tumors from each group and (b) the tumor mass. $^{*}p < 0.05$; $^{**}p < 0.005$.

(A)

(B)

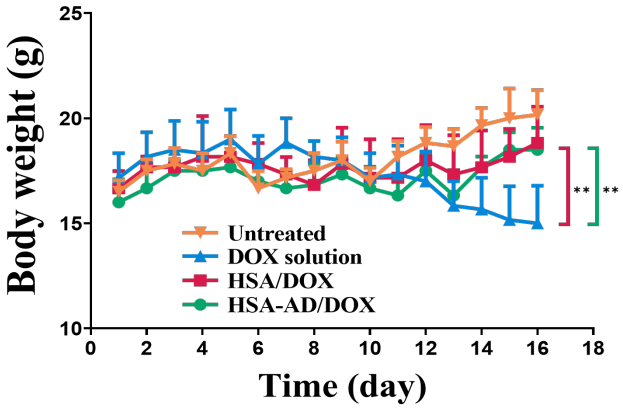

Figure 33. Investigation of body weight change in the mice for 16 days. (a) Representative image of each group on day 16 and (b) average body weight change. $^{**}p < 0.005$.

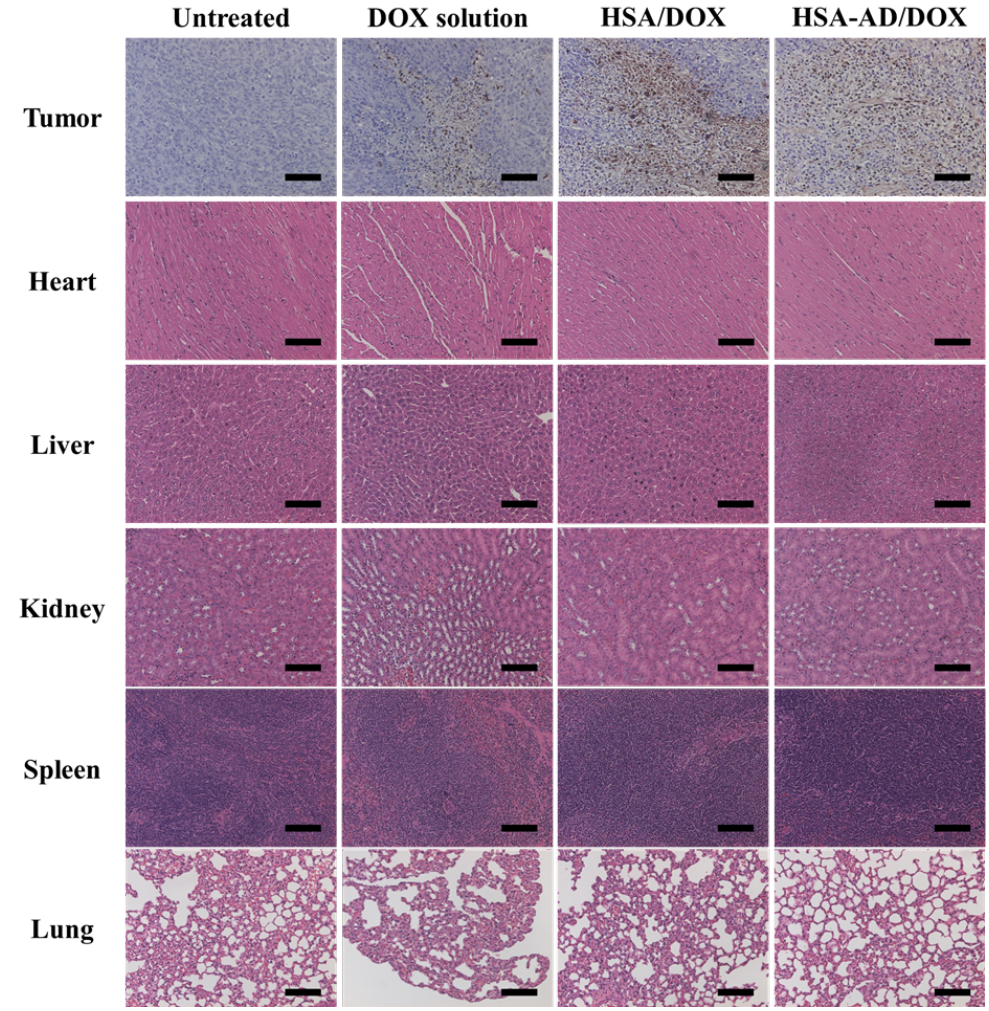

Figure 34. Histological analysis of the dissected tumors and major organs on day 16. The tumors and organs were stained with TUNEL and H&E, respectively.

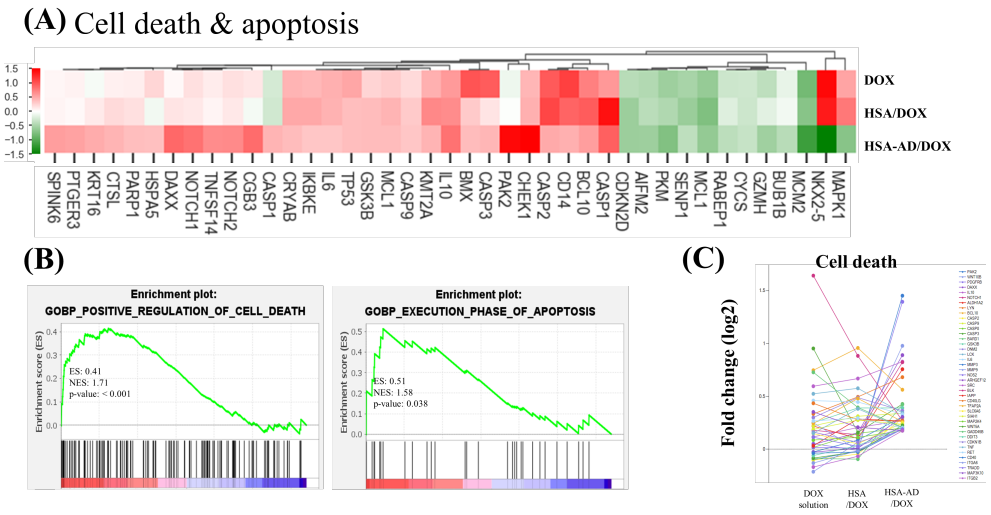

Figure 35. Protein expression pattern of the formulation-treated tumors. (a) Heatmap of cell death-and apoptosis-related protein expression compared to the untreated group. (b) GSEA of HSA-AD/DOX group. (c) Core-protein expression plots related to cell death.

국문 초록

골 암은 뼈와 유사한 세포 외 기질을 특징으로 한 종양 미세 환경을 특징으로 하며, 이는 항암치료 효과를 떨어뜨리는 주요 원인으로 평가된다. 본 연구의 목표는 골 암의 미세환경의 주요 성분 중 하나인 하이드록시아파타이트에 대한 표적성을 높여 암으로의 약물 분포를 증가시키고 항암 활성이 증가된 알부민 기반 나노 전달체를 개발하는 것이다. 이를 위해 알렌드로네이트를 알부민 표면에 수식하였으며, 새롭게 개발한 Ball-milling technology (BMT) 방식을 도입하여 독소루비신을 표면에 흡착시킴과 동시에 나노클러스터를 형성하도록 디자인하였다. 제조된 나노 클러스터는 알부민의 2차 구조를 90 % 이상 유지하였으며, 신생혈관의 알부민 수용체에 대한 친화력이 유지되는 것을 *in vitro* 세포 실험 수준에서 확인하였다. 암세포 및 하이드록시아파타이트에 대한 표적성은 골 암의 미세 환경을 모방하는 세포 실험계에서 평가되었으며, 증가된 암세포 흡수율과 하이드록시아파타이트 결합능이 확인되었다. 나노클러스터의 하이드록시아파타이트에 대한 증가된 표적성은 유세포 분석기 및 자외 및 가시선 분광분석법을 통해 HSA-AD/DOX 의 경우 HSA/DOX에 비해 5.04배 높은 친화력을 보이는 것을 확인하였다. 이를 기반으로 골 암 조직으로의 분포를 *in vivo* 상에서 검증하기 위해 암세포와 하이드록시아파타이트가 혼합되어 주입된 이종이식 마우스 모델을 구축하여 평가하였다. HSA-AD/DOX는 HSA/DOX에 비해 52% 가량 증가된 암 조직 분포를 보였으며, 암 조직의 조직학적 분석을 통해 하이드록시아파타이트에 대한 높은 친화력이 원인임을 증명하였다. 본 모델에서의 항암활성 평가를 진행하였을 때, 독소루비신 수용액 및

HSA/DOX에 비해 더욱 적은 독성으로 암세포의 성장을 유의미하게 감소시킨 것으로 평가되었다. 항체를 이용한 마이크로어레이 기법을 도입하여 제형 처리 후 암세포 내 세포사멸 관련 단백질의 발현패턴을 관찰 및 GSEA 분석하였으며, HSA-AD/DOX에서 통계적으로 유의미한 관련성을 확인하였다. 조직 독성은 주요 장기의 조직학적 평가 및 전혈 분석을 통해 평가하였으며, DOX 수용액 그룹에 비해 유의미한 심장 및 전신 독성 감소를 확인하였다. 본 연구의 결과들을 종합하여 평가할 때, 새롭게 개발된 알렌드로네이트가 수식된 알부민 기반 나노입자는 골 암 치료에 효과적이고 안전성이 증가된 것을 확인하였다.

주요어: 골 암, 알렌드로네이트, 사람 혈청 알부민, 나노클러스터, 하이드록시아파타이트

학 번: 2016-22653